Single Electron Capture from Atomic and Molecular Collisions Using

Advanced Theoretical Methods

by

David Lyons

(Under the Direction of Philip Stancil)

Abstract

Cross sections for single electron capture (SEC), or charge exchange (CX), in collisions of $Ne^{(8-10)+}$ and $Mg^{(8-12)+}$ with H and He, and $Fe^{(8-9)+}$ with H, H_2, He, H_2O, CO, CO_2, and N_2, are computed using an approximate multichannel Landau-Zener (MCLZ) formalism. The Molecular Orbital Close-Coupling (MOCC) method is also used for the cross section calculation of the Ne^{9+}+H collision system. Final-state-resolved cross sections for the principal (n), orbital angular momentum (ℓ), and where appropriate, total spin angular momentum (S) quantum numbers are explicitly computed except for the incident bare ions Ne^{10+} and Mg^{12+}. In the latter two cases, $n\ell$-resolution is obtained from analytical ℓ-distribution functions applied to n-resolved MCLZ cross sections. In all cases, the cross sections are computed over the collision energy range 1 meV/u to 50 keV/u with LZ parameters estimated from atomic energies obtained from experiment, theory, or, in the case of high-lying Rydberg levels, estimated with a quantum defect approach. Errors in the energy differences in the adiabatic potentials at the avoided-crossing distances give the largest contribution to the uncertainties in the cross sections, which is expect to increase with decreasing cross section magnitude. The energy differences are deduced here with the Olson-Salop-Tauljberg radial coupling model. Proper selection of an ℓ-distribution function for bare ion collisions

introduces another level of uncertainty in the results. Comparison is made to existing experimental or theoretical results when available, but such data are absent for most considered collision systems. The $n\ell S$-resolved SEC cross sections are used in a optically thin cascade simulation to predict X-ray spectra and line ratios which will aid in modeling the X-ray emission in environments where charge exchange is an important mechanism. Details on a MCLZ computational package, *Stüeckelberg*, are also provided.

<div>

INDEX WORDS: Atomic Data, Atomic Processes, Charge Exchange, Single Electron
Capture, Molecular Collisions, Atomic Collisions, Ionic Collisions,
Cross Sections, Landau-Zener, Molecular Orbital Close Coupling,
Numerical Simulation

</div>

Single Electron Capture from Atomic and Molecular Collisions Using

Advanced Theoretical Methods

by

David Lyons

BS, Electrical Engineering, Southern Illinois University

MS, Electrical Engineering, Southern Illinois University

MBA, University of Georgia

MS, Physics, University of Georgia

A Dissertation Submitted to the Graduate Faculty

of The University of Georgia in Partial Fulfillment

of the

Requirements for the Degree

Doctor of Philosophy

Athens, Georgia

2019

Single Electron Capture from Atomic and Molecular Collisions Using

Advanced Theoretical Methods

by

David Lyons

Approved:

Major Professor: Philip Stancil

Committee: Henning Meyer
Loris Magnani

Electronic Version Approved:

Suzanne Barbour
Dean of the Graduate School
The University of Georgia
May 2019

To the memory of Jeff Burns and his family. In my opinion, the world would have been a better place if Jeff had lived longer. But I denied the world of that priveledge. Therefore, the responsibility of "taking up the slack" is my burden. Thus, I must use whatever abilities I possess to produce something positive and useful in this world to make up for what I took away from it. I owe the world.

Acknowledgments

TABLE OF CONTENTS

INTRODUCTION

With continual improvements in X-ray detector technology from charge-coupled devices (CCDs) to the reflection grating spectrometer (RGS) available on the current fleet of X-ray satellites (*Chandra, XMM-Newton, Suzaku*), the resolution of X-ray spectra have dramatically improved allowing for detailed studies of line formation mechanisms. While X-ray lines from highly ionized plasmas are primarily produced by electron impact excitation (EIE) in collisionally ionized equilibrium (CIE) or via electron radiative recombination (RR) in photoionized environments, a third mechanism, charge-exchange (CX) induced X-ray emission, has been found to be important in situations where hot plasmas meet cold gas.

The importance of CX as a mechanism for producing X-ray emission was recognized from studies of the Jovian aurora as early as the 1980s (e.g., Cravens et al. 1995, and references therein), but it was the detection of cometary X-ray emission (Lisse et al. 1996), and later its possible contribution to the soft X-ray background (Cox 1998; Cravens 2000) which brought CX induced emission to the attention of the high-energy astrophysics community. More recently, CX has been invoked for a host of environments, from supernova remnants (Katsuda et al. 2011; Cumbee et al. 2014, 2016) to extragalactic cooling flows (Fabian et al. 2011), in attempts to explain "anomalous" X-ray emission features which are unlikely to be attributable to EIE or RR. Unfortunately, the current CX cross sectional data are of insufficient reliability or availability to allow for quantitative spectroscopic models. To partially address this situation, cross sections, as a function of kinetic energy, for a series of single electron capture (SEC) collision systems are calculated here using the multi-channel Landau-Zener (MCLZ) (Janev et al. 1983; Butler and Dalgarno 1980) and Molecular Orbital

Close-Couplng (MOCC) methods. Theoretical summaries of these methods are presented in Chapter 2.

Chapter 3 discusses the study of $Ne^{(10-8)+}$ and $Mg^{(12-8)+}$ colliding with neutral H and He resulting in single electron capture. The resulting cross sections are calulated over a range of energies from 10^{-1}–10^5 eV/u. The MCLZ method is used since it is reasonably accurate for kinetic energies $\lesssim 10$ keV/u, and computation effort is minimal which allows several collision systems to be studied, benchmarking their results to other data when available. In many of these cases, explicit experimental or theoretical CX data are lacking. Collisional ionization, not included in the MCLZ model, begins to become important, and eventually dominates, at higher energies.

Chapter 4 discusses $Fe^{(9-8)+}$ in collisions with H, H_2, He, H_2O, CO, CO_2, and N_2. For the same reasons with with Ne and Mg, the MCLZ is used to calculate the cross sections of collisions over a range of energies from 10^{-1}–10^5 eV/u. For Fe^{9+}, multiple calculations are performed on each collision system as dictated by Wigner-Witmer rules (Wigner and Witmer 1928) describing the symmetries of the scattering channels. Cross section calculations are performed for singly-excited $n\ell$-resolved quantum states. Cross sections are also calculated for core-excited states when those energies are available. Excitation energies are estimated only for singly-excited states when they are not initially available.

SEC cross sections for these collision systems—$Fe^{8+}+H_2O$, $Fe^{9+}+H_2O$, $Fe^{8+}+CO$, $Fe^{9+}+CO$, $Fe^{8+}+CO_2$, and $Fe^{9+}+CO_2$—are found in only two publications Simcic et al. (2010a) & Simcic et al. (2010b), which provide cross sections from experimental and n-electron classical trajectory Monte Carlo (nCTMC) methods at $7q$ keV. This study produces results which can serve as a basis of comparison for any future studies of these systems. The cross sections produced here can be used for further prediction of X-ray spectra where these systems may be found, such as in the solar wind, comets, and supernova remnants (Cumbee et al. 2016; Lyons et al. 2017).

In Chapter 5, Ne^{9+}+H is studied using MOCC. Cross sections comparision are made with existing data and discussed.

Conclusions are given in Chapter 6. An Appendix discusses the implementation of the MCLZ method in a new computational package, *Stüeckelberg*. Atomic units are used unless otherwise indicated.

CHAPTER 2

THEORY

2.1 CHARGE EXCHANGE

The interaction of two particles where single electron capture charge exchange occurs can be described by

$$X^{q+} + Y(1s) \rightarrow X(n, \ell)^{(q-1)+} + Y^+ + \Delta E, \tag{2.1}$$

where X is a positively charged ion, Y is a neutral atom or molecule, q is the ionic charge, n is the principal quantum number, ℓ is the angular momentum quantum number, and E is energy.

In the Landau-Zener model, the difference between ionization potential of the two particles can be written as

$$\Delta E = I(X^{(q-1)+}) - I(Y) \tag{2.2}$$

The polarization potential of the dominant long-range interaction bewteen X and Y is

$$V_p = \frac{\alpha q^2}{2R^4} \tag{2.3}$$

where R is the separation, or internuclear distance, in atomic units, and α is the polarizability of the neutral target Y. According to Schwerdtfeger and Nagle (2018), if Y=H (hydrogen), then α=4.5. And if Y=He (helium), then α=1.383191.

$$V_c = \frac{q-1}{R} \tag{2.4}$$

Plots of equations 2.2, 2.3, and 2.4 are shown in Figure 2.1.

4
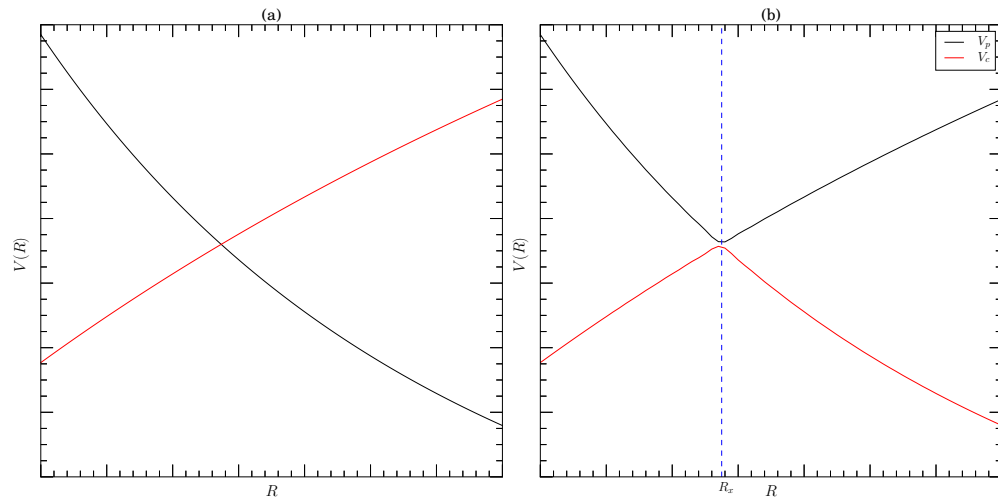
Figure 2.1 Polarization (V_{p}) and Coulomb (V_{c}) potentials: (a) diabatic crossing; (b) adiabatic avoided crossing at R_x.

Ne$^{(8-10)+}$ and Mg$^{(8-12)+}$ with H and He using MCLZ[1]

3.1 Methods

Many physical phenomena can be modeled by a two-level system (TLS) consisting of two interacting states (Nakamura 2002). The strength of the interaction can be varied typically by some external parameter such that the internal state energies of the quantum TLS exhibit an avoided-level crossing. Some physical property of the two states is typically exchanged when passing from one side of the avoided crossing to the other. In such a case, the system undergoes a nonadiabatic transition between the two energy states. Nonadiabatic interactions were first discussed by Landau (1932), Zener (1932), and Stüeckelberg (1932). In the current study, the control parameter is the distance R between an incident ion and a target neutral which interact during a charge exchange collision process (Equation 2.1), where an electron is transferred from the neutral target to an highly-ionized ion. Application of a TLS analysis to charge transfer systems is commonly referred to as the Landau-Zener (LZ) method. Here we apply a series of TLS crossings via the LZ approach of Butler and Dalgarno (1980) with the multichannel formalism of Janev et al. (1983).

For all collision systems, the first step in the MCLZ approach is to estimate the avoided crossing distances R_x between the incoming and outgoing channels. Beginning with atomic energies available from the NIST Atomic Spectral Database (Kramida et al. 2018), the crossings are estimated and then used to predict the adiabatic potential splitting at the crossing, $\Delta U(R_x)$, using the Olson and Salop (1977) radial coupling model for product

hydrogen-like ions. In the case of multielectron ions, the Olson-Salop-Tauljberg (Tauljberg 1986) radial coupling approximation is adopted. The rotational coupling model of Janev et al. (1983) is included for hydrogen-like product ion systems, but only the radial coupling is considered for multielectron ions. In addition to R_x and $\Delta U(R_x)$, a third LZ parameter, the difference in slopes of the diabatic potentials at R_x is obtained analytically from empirical molecular potentials for the collision complexes following Butler and Dalgarno (1980).

In most cases, each individual $n\ell$ or $n\ell S$-resolved SEC cross section is calculated directly with the MCLZ method. However, if the ion is initially bare, then the SEC cross sections for the angular momentum states in each n-shell are estimated using analytical ℓ-distribution functions (see, for example, Krasnopolsky et al. 2004; Smith et al. 2014). ℓ-distribution functions are necessary in such cases due to the ℓ-level degeneracy in a given n-manifold. Unfortunately, this introduces considerable uncertainty in the $n\ell$-resolved cross sections as will be illustrated below.

Here, statistical distribution function is considered,

$$W_{nl}^{st} = \frac{2l+1}{n^2}, \tag{3.1}$$

and the low-energy distribution (Abramov et al. 1978; Krasnopolsky et al. 2004),

$$W_{nl}^{le} = (2l+1)\frac{[(n-1)!]^2}{(n+1)!(n-1-l)!}. \tag{3.2}$$

The statistical distribution function is believed to be valid for energies above $\sim$5–10 keV/u, while for lower energies, the low-energy distribution function is preferred (Krasnopolsky et al. 2004; Cumbee et al. 2016; Mullen et al. 2016).

For some ions, experimental or theoretical energy level data for high-lying Rydberg states are lacking. In such instances, the ion energies are estimated with a variant of the quantum defect method (Connerade 1998; Mullen et al. 2016) and polynomial extrapolations from available energy data (Kramida et al. 2018). While advanced atomic structure calculations

can be performed, the goal is to utilize available recommended data with quick extrapolations.

3.2 SINGLE ELECTRON CAPTURE CROSS SECTIONS
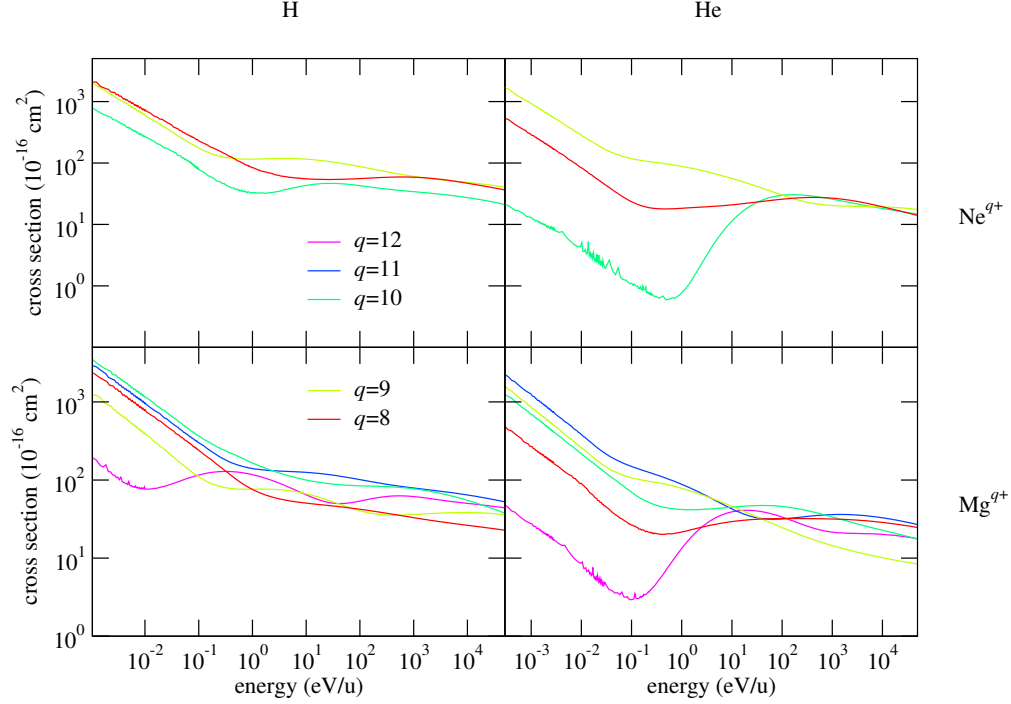
Figure 3.1 Total single electron capture cross sections for Ne^{q+} and Mg^{q+} collisions with hydrogen (H) and helium (He) for q=8–12 obtained with the MCLZ method.

Total MCLZ charge exchange cross sections for all systems studied are presented in Figure 3.1. The total cross sections for both H and He targets generally converge at high collision energies to within a factor of $\sim$5, but diverge for $E \lesssim 1-10$ eV/u. At low kinetic energies, all cross sections go to the Langevin limit, increasing as $1/E^{1/2}$ with decreasing kinetic energy. Collisions with bare ions give the smallest cross sections since the interaction results in a smaller number of final channels, degenerate for a given n. Details on each collision system are given below with comparison to available theoretical or experimental results.

3.3 NE^{10+}

Of all the ions considered here, Ne^{10+} has received the most attention, being the subject of numerous theoretical and experimental studies for the past 40 years. Unfortunately, this is not the case for most of the other ion-atom collision systems.
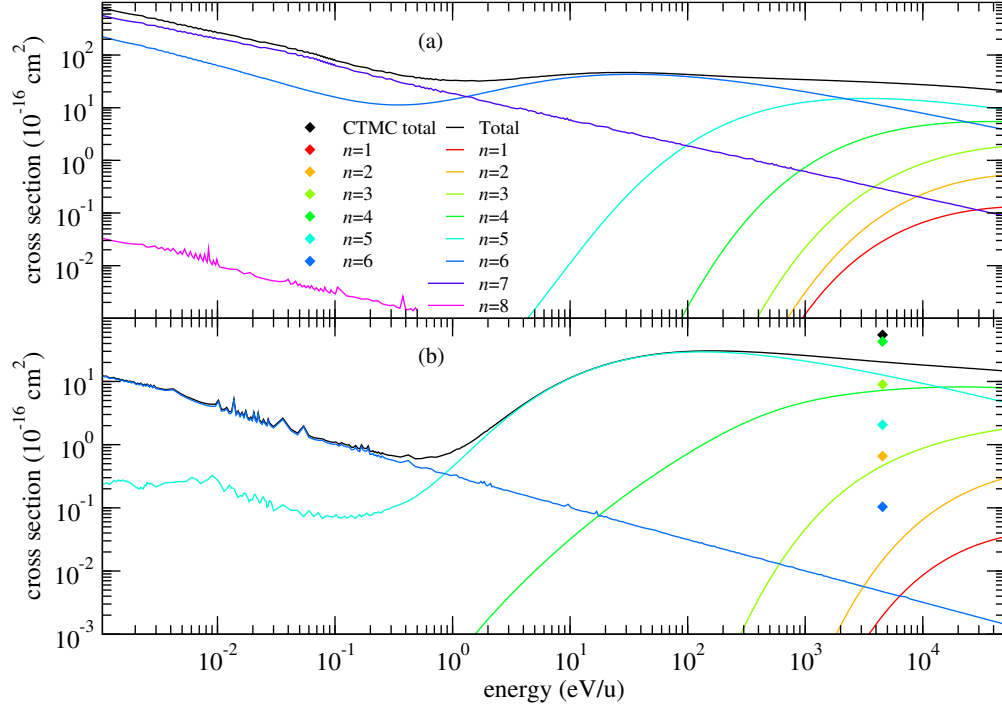
Figure 3.2 MCLZ n-resolved and total single electron capture cross sections for (a) Ne^{10+}+H and (b) Ne^{10+}+He and comparison to the CTMC cross sections of Ali et al. (2010).

The total and n-resolved MCLZ SEC cross sections for Ne^{10+}+H and Ne^{10+}+He are presented in Figure 3.3. Comparison is made in the latter at 4.5 keV/u, to the CTMC results of Ali et al. (2010) where general agreement is seen with the current MCLZ calculations, both indicating that the dominant capture channels are n=3, 4, and 5, but with different ordering. This is not unexpected given that the MCLZ method is approaching its range of applicability at our high energy limit, while the CTMC results approach their low energy

9

validity range (i.e., the uncertainty in both CTMC and MCLZ are expected to be relatively high at this collision energy).
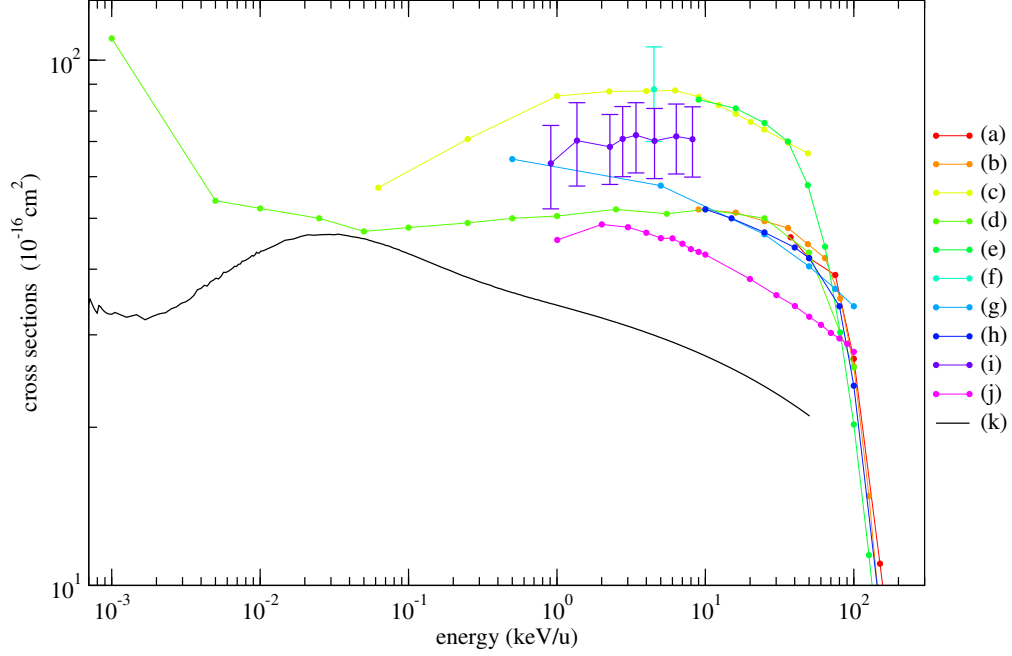
Figure 3.3 $Ne^{10+}+H$ single electron capture cross section comparison: (a) CTMC (Olson and Salop 1977); (b) CTMC microcanonical (Errea et al. 2004); (c) OEDM (Errea et al. 2004); (d) CTMC (Perez et al. 2001); (e) CTMC hydrogenic (Errea et al. 2004); (f) experimental (Bendahman et al. 1985); (g) theory (Grozdanov 1980); (h) CTMC (Maynard et al. 1992); (i) experimental (Meyer et al. 1985); (j) CTMC (Schultz and Kristić 1996); and (k) current MCLZ.

In Figure 3.3, the total MCLZ cross section for $Ne^{10+}+H$ is compared to other calculations and experimental data. While there is a large dispersion in the data between 1 and 50 keV/u, it can be seen that the MCLZ results are very close to those obtained with CTMC (Perez et al. 2001) over the range 10-100 eV/u. For higher energies, the MCLZ results underestimate the available data, being about a factor of 2 smaller than the measurements of Meyer et al. (1985), possibly due to the neglect of short-range avoided-crossings.
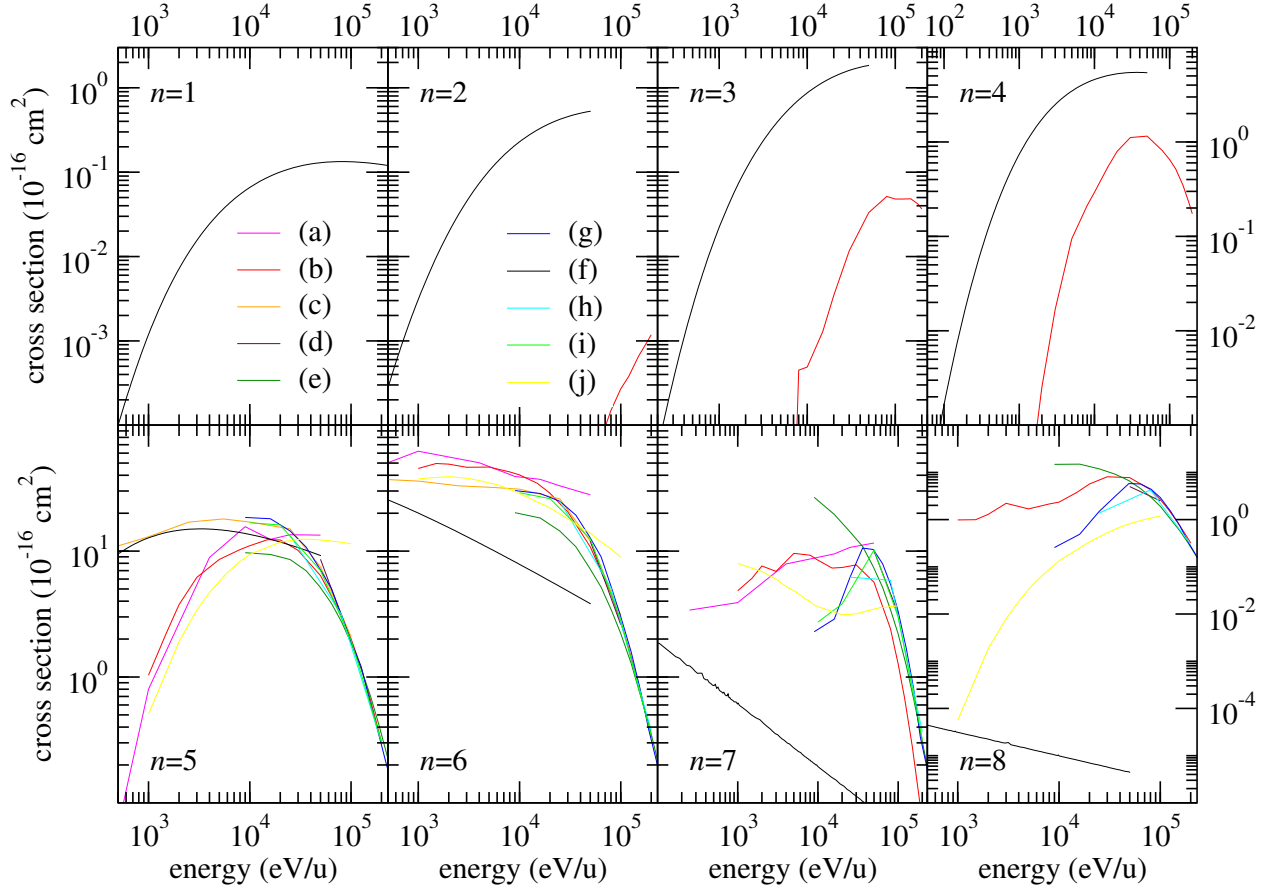
Figure 3.4 $Ne^{10+}+H$ (n-resolved) single electron capture cross section comparison: (a) Bendahman et al. (1985); (b) AOCC (Cumbee et al. 2016); (c) CTMC (Perez et al. 2001); (d) CTMC (Olson and Salop 1977); (e) CTMC hydrogenic (Errea et al. 2004); (f) current MCLZ; (g) CTMC microcanonical (Errea et al. 2004); (h) CTMC (Maynard et al. 1992); (i) OEDM (Errea et al. 2004); (j) CTMC (Schultz and Kristić 1996).

MCLZ n-resolved cross sections are also compared to available data, as presented in Figure 3.4. For each cross section, there are AOCC data available for comparison (Cumbee et al. 2016), but in the cases of $n=1$ and $n=2$, the AOCC cross sections are significantly smaller, being off the scale of the plots. For $n=4$, the MCLZ cross section comes within an order of magnitude of the AOCC calculation. While for $n=5$ and $n=6$, the MCLZ and AOCC cross sections overlap at higher energies. Compared to other data, $n=5$ gives the closest agreement, especially around 20-30 keV/u compared to the measurements of

11

Bendahman et al. (1985) and the CTMC calculations of Perez et al. (2001). The results for $n=6$ are somewhat smaller than all previous results, while the $n=7$ and 8 cross sections are underestimates, again due to the lack of short-range couplings in the MCLZ model. The underestimation of the MCLZ $n=6$ cross section accounts for most of the discrepancy in the total cross section given in Figure 3.3.
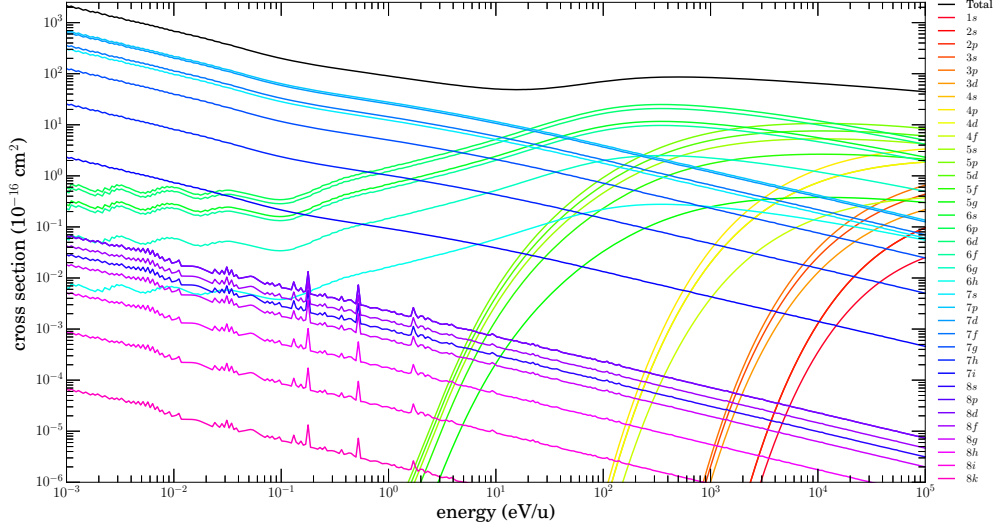
Figure 3.5 Ne^{10+}+H→Ne^{9+}+H$^+$ $n\ell$-resolved cross sections using the low-energy distribution function.
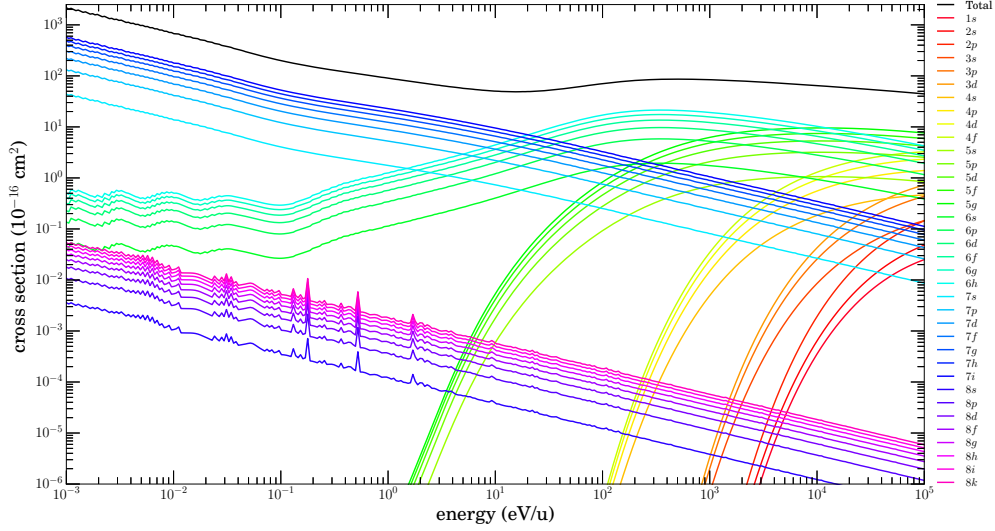
Figure 3.6 $Ne^{10+}+H\rightarrow Ne^{9+}+H^+$ $n\ell$-resolved cross sections using the statistical distribution function

For $Ne^{10+}+H$, the $n\ell$-resolved cross sections are calculated using the low-energy (Figure 3.5) and statistical (Figure 3.6) distribution functions. CTMC data from Schultz and Kristić (1996) are compared to MCLZ $n\ell$-resolved cross sections for $n=5$, $n=6$, and $n=7$ for the low-energy (Figure 3.7) and statistical (Figure 3.8) distribution functions. For $n=4$ and $n=5$, the cross sections are within an order of magnitude of those of Schultz and Kristić (1996). In fact, in the lower range of the data, $n=4$ is very similar to Schultz and Kristić (1996), and in the $n\ell$-resolved case, they can be seen to be in close agreement. However, Figure 3.7 (b) shows the correspondence between the ℓ states of each method to be out of order. The MCLZ states, from highest to lowest are ordered: d, p, s, f, and g, while for Schultz and Kristić (1996), they are arranged as: g, f, d, p, and s, i.e., the latter follow a statistical distribution, though it is expected that for energies less than 1 keV/u, the ℓ distribution should follow more closely the low-energy distribution form. A similar phenomenon appears in graphs (c) and (d). As a consequence, the MCLZ $n\ell$-resolved statistical cross sections, as shown in Figure 3.8, are in better agreement with the CTMC results (Schultz and Kristić 1996), as might be expected. It should be noted that 10 keV/u corresponds to the region where the

applicability of both methods, MCLZ and CTMC, begins to be questionable, i.e. MCLZ is expected to be reliable for lower kinetic energies and CTMC for higher energies, likewise, the statistical ℓ-distribution is likely valid at 10 keV/u, while the low-energy distribution may be expected to be reasonable below 1 keV/u. How the transition should be made from statistical to low-energy, and at what kinetic energy, is unknown.
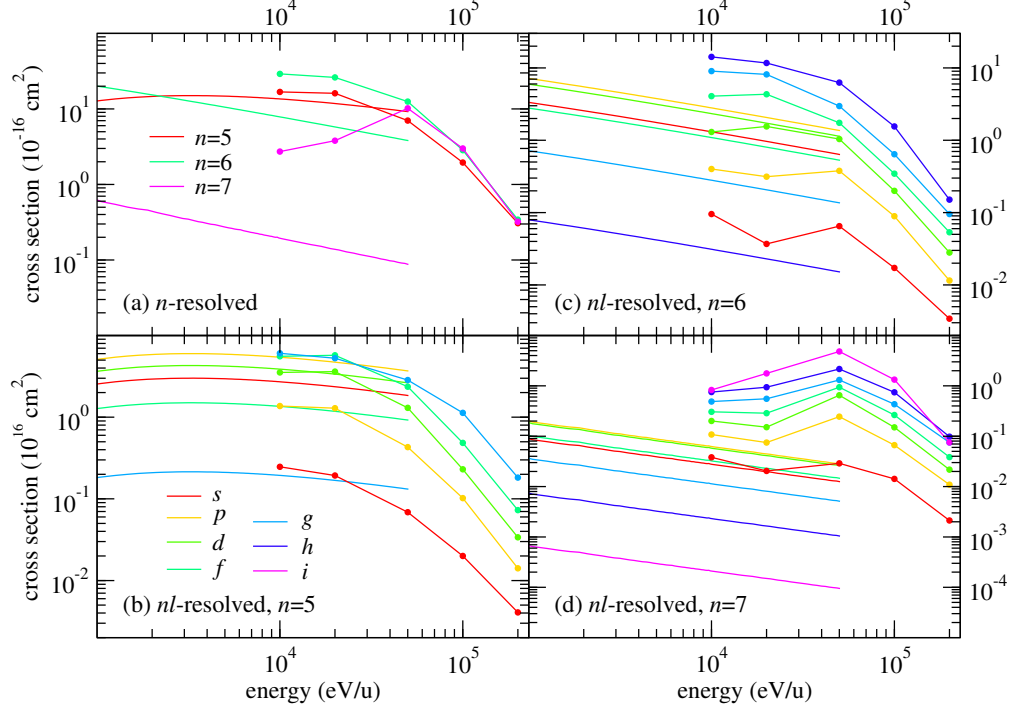
Figure 3.7 Ne^{10+}+H cross section comparisons; MCLZ low-energy distribution function (lines) & CTMC (Schultz and Kristić 1996) (lines with circles).
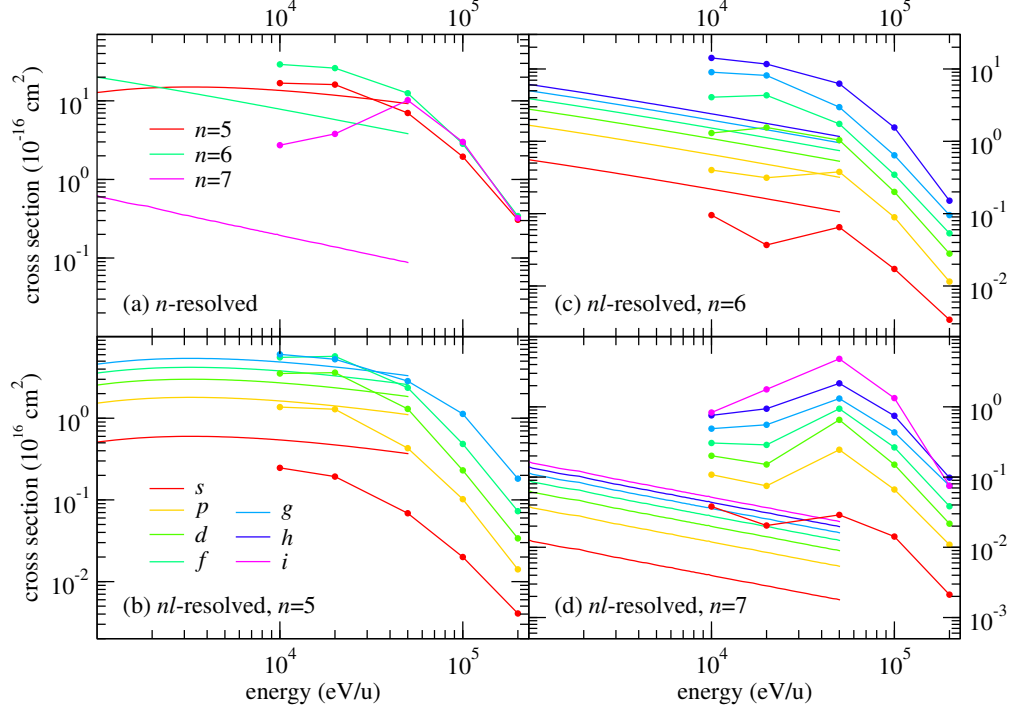
Figure 3.8 Ne^{10+}+H cross section comparisons; MCLZ statistical distribution function (lines) & CTMC (Schultz and Kristić 1996) (lines with circles).

MCLZ $n\ell$-resolved cross sections for Ne^{10+}+He are presented in Figure 3.5 (low-energy distribution function) and Figure 3.6 (statistical distribution function). Comparison to CTMC results at 4.5 keV/u are given in Figure 3.3(b). The ordering of the n-resolved cross sections shows considerable discrepancies, but the MCLZ results are found in Cumbee et al. (2016) to be in excellent agreement with the experimental X-ray emission spectrum of Ali et al. (2010). It is therefore expected that the MCLZ $n\ell S$ cross sections are reliable in this case to better than 10.

3.4   NE^{9+}
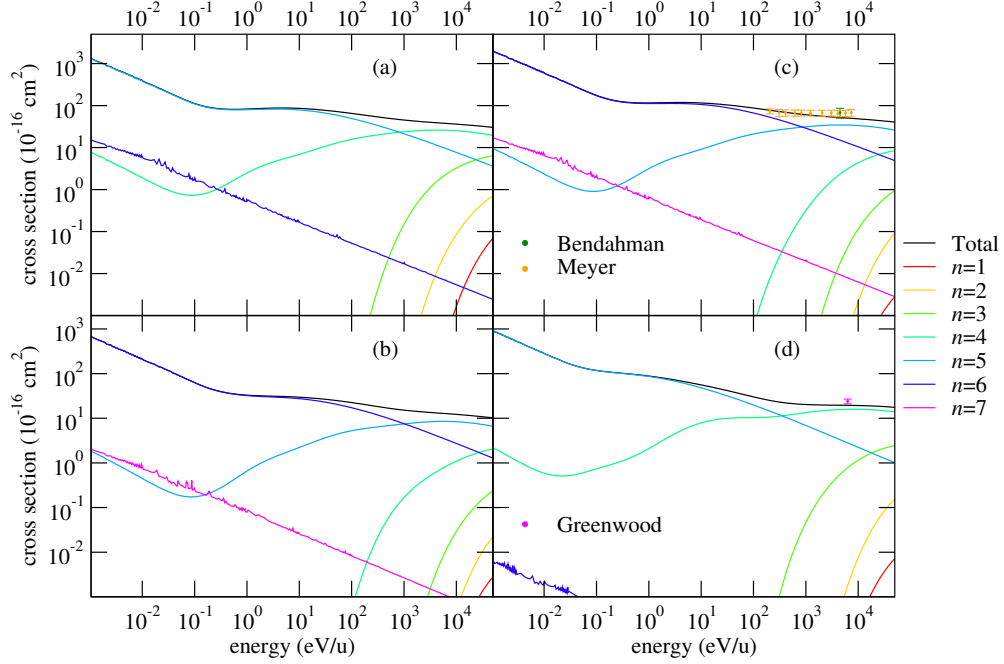
Figure 3.9 Ne^{9+}+X→Ne^{8+}+X^+ MCLZ n-resolved cross sections. (a): X=H (triplets); (b): X=H (singlets); (c) X=H (sum of singlets and triplets) and experimental data (Bendahman et al. 1985; Meyer et al. 1985); (d) X=He, n-resolved, and comparison to experiment of Greenwood et al. (2001).

For Ne^{9+}+H, the singlet and triplet cross sections are calculated separately due to symmetry considerations. Figure 3.9 (a) shows the n-resolved triplet cross sections, where the dominant capture channel is n=5 (for energies above 1 keV/u), and n=6 for energies below that value. In (b), the n-resolved singlet cross sections are similar. Graph (c) shows the total n-resolved cross sections, which are the sums of each n state in the singlets and triplets, and they are compared to experimental total cross section data from Bendahman et al. (1985) and Meyer et al. (1985). The MCLZ cross section is in close agreement with results of both Bendahman et al. (1985) and Meyer et al. (1985). Figure 3.9 (d) shows the single electron capture n-resolved cross sections for Ne^{9+}+He, with comparison to the single measurement of Greenwood et al. (2001). The latter is also in excellent agreement with the MCLZ results.
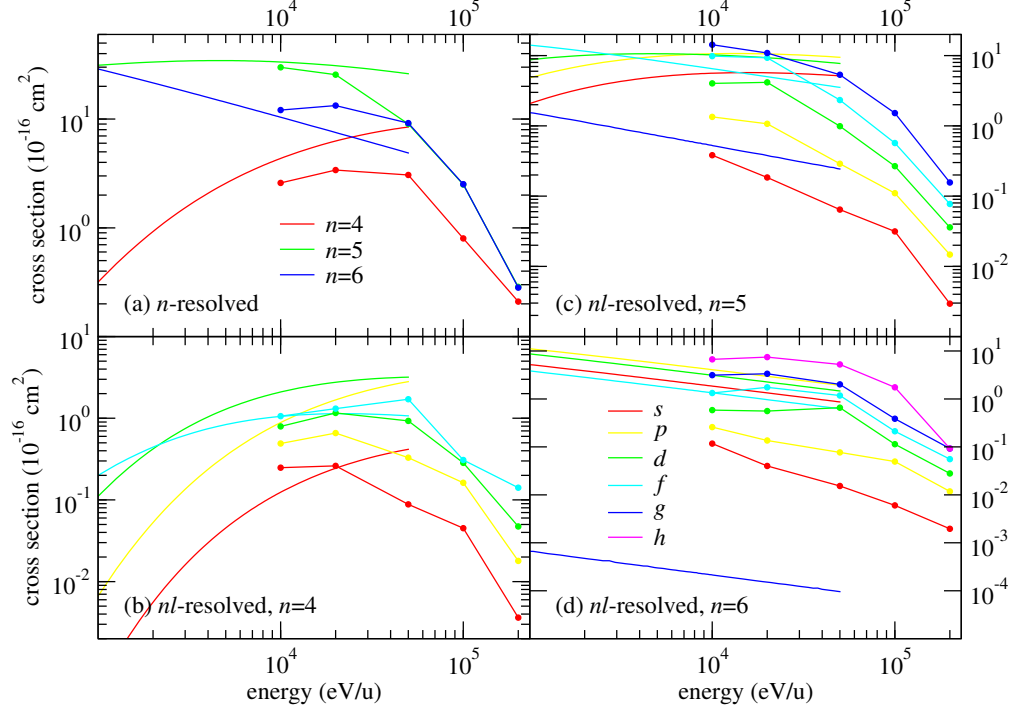
Figure 3.10 Ne^{9+}+H cross section comparisons; MCLZ (lines): CTMC (Schultz and Kristić 1996) (lines with circles). Note that ℓ-distribution functions are not needed for two or more electron ions for MCLZ calculations.

Figure 3.10 displays a comparison of MCLZ $n\ell$-resolved cross sections for Ne^{9+}+H with CTMC data (Schultz and Kristić 1996). The data are in good agreement with each other at 10 keV/u for the n-resolved cross sections, but they diverge at higher energies as would be expected. Further, the CTMC calculations adopt an effective one-electron model and cannot distinguish final singlet or triplet ions. As a consequence, CTMC results generally follow a statistical ℓ-distribution pattern. On the other hand, each $n\ell S$-cross section is explicitly calculated, without a distribution function, with the MCLZ method. Further, for He-like ions, the degeneracy in an n-manifold is lifted, but the energy of the states may be in a counter-intuitive order. As an example, the 4 ^{3}L ordering is S, P, F, and D, which partially explains the same ordering in the MCLZ cross sections about ~2 keV/u in Figure 3.10(b).

3.5 Ne^{8+}
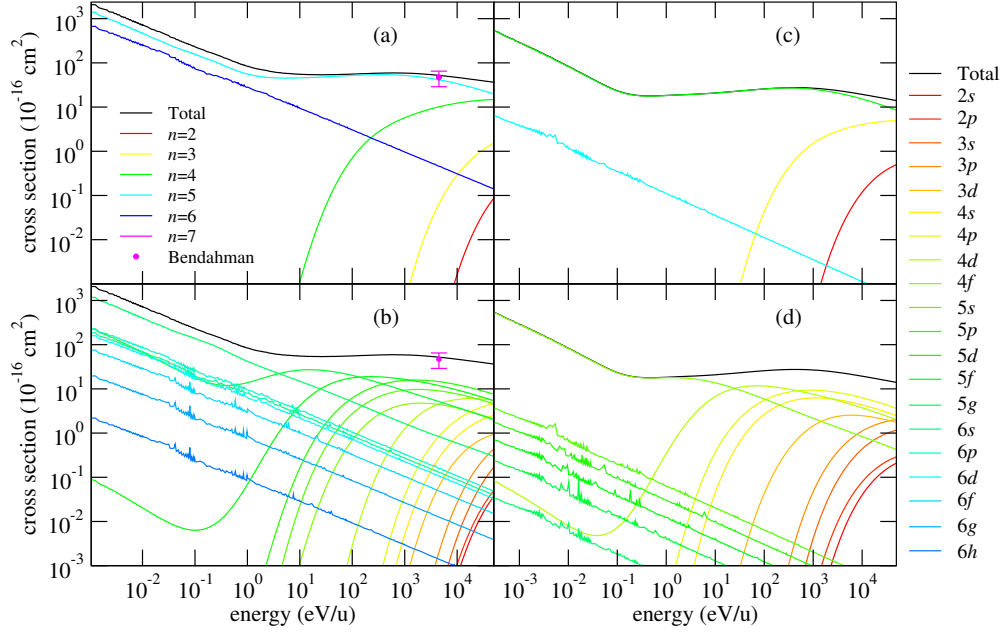
Figure 3.11 Ne^{8+} MCLZ single electron capture cross sections. (a) H (n-resolved), and experimental data (Bendahman et al. 1985); (b) H ($n\ell$-resolved); (c) He (n-resolved); (d) He ($n\ell$-resolved).

Ne^{8+}+H and Ne^{8+}+He cross sections, n- and $n\ell$-resolved, are presented in Figure 3.11. For comparison purposes, there is also an experimental data point from Bendahman et al. (1985), which agrees with the MCLZ total cross section at 10 keV/u.
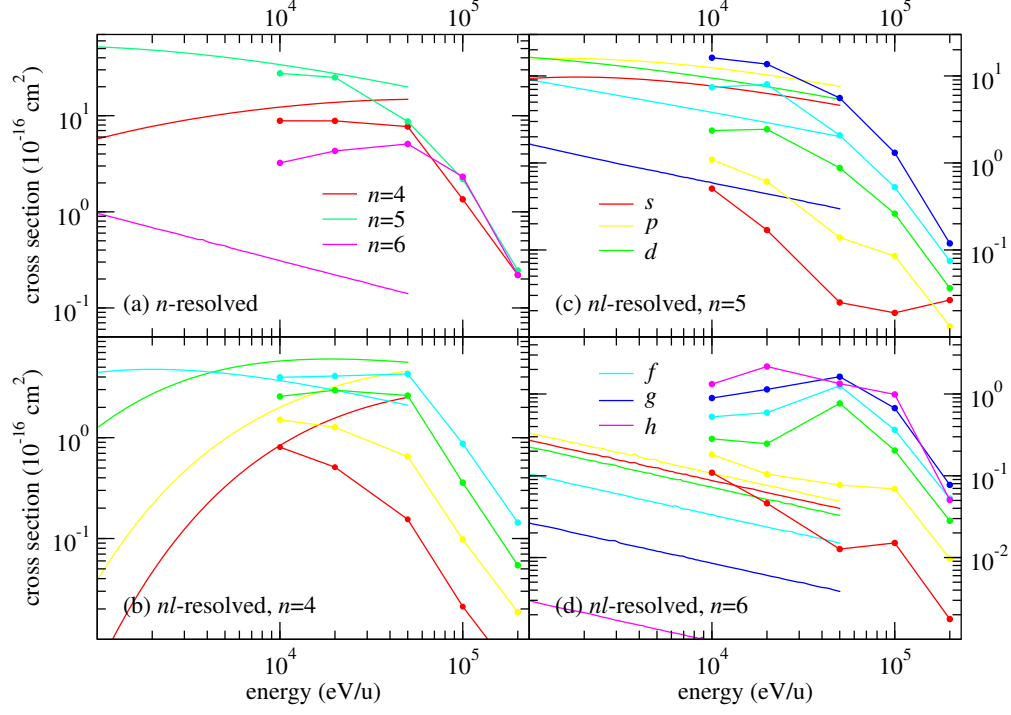
Figure 3.12 Ne^{8+}+H cross section comparisons; MCLZ (lines): MCLZ; CTMC (Schultz and Kristić 1996) (lines with circles).

Figure 3.12 shows a comparison of MCLZ n- and $n\ell$-resolved cross sections with CTMC data (Schultz and Kristić 1996). At 10 keV/u, n=4 and n=5 closely agree with the CTMC results from Schultz and Kristić (1996). For the $n\ell$-resolved cross sections in (b), the agreement at 10 keV/u is very good since the effective one-electron CTMC model should be valid for the Li-like Ne product ions. However, as for Ne^{9+} collisions, the CTMC ℓ-distributions are statistical, while MCLZ ℓ-cross section orders are controlled mostly by the energy ordering of states.

3.6   Mg^{12+}

Total cross sections for Mg^{12+} with H and He are shown in Figure 3.13.
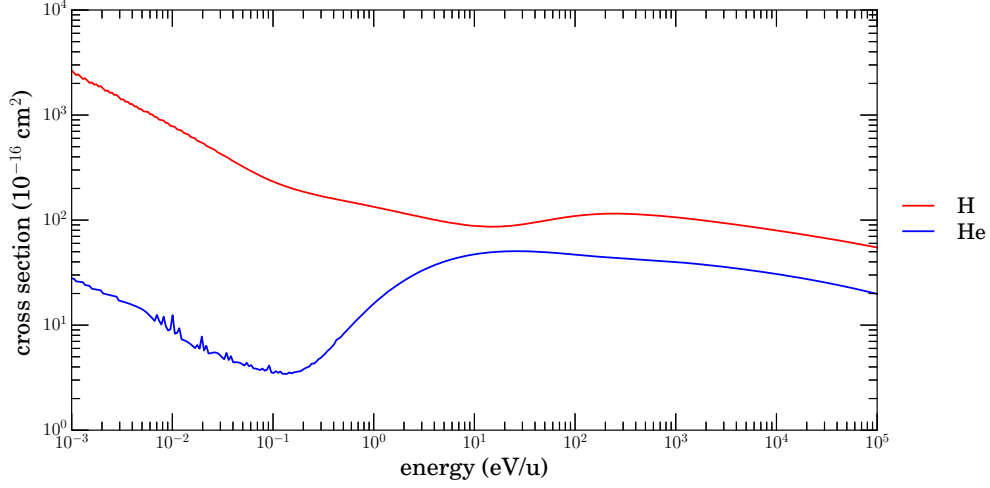
Figure 3.13 $Mg^{12+}+X \rightarrow Mg^{11+}+X^+$ total cross sections.

The $n\ell$-resolved cross sections are calculated using the statistical (Equation 3.1) and low-energy (Equation 3.2) distribution functions. Plots for these results are shown in the appropriate sections below. Furthermore, previously published results for Mg^{12+} ionic collisions with H and He are not available. The results here can server as a basis for future comparisons.

3.6.1   H

Figure 3.14 shows the n-resolved cross sections for $Mg^{12+}+H \rightarrow Mg^{11+}+H^+$. The dominant channels, as shown in the figure, are listed in Table 3.10.2.
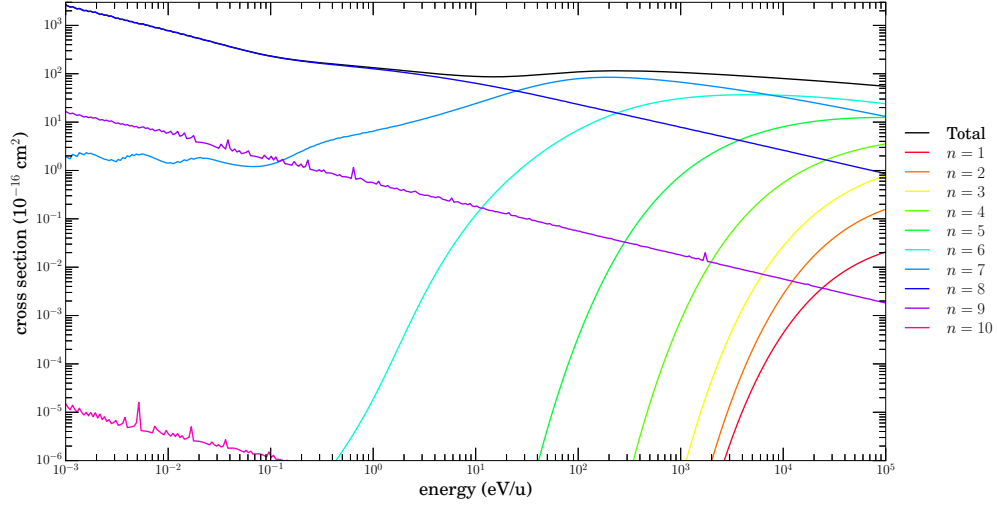
Figure 3.14 Mg^{12+}+H→Mg^{11+}+H$^+$ n-resolved cross sections.
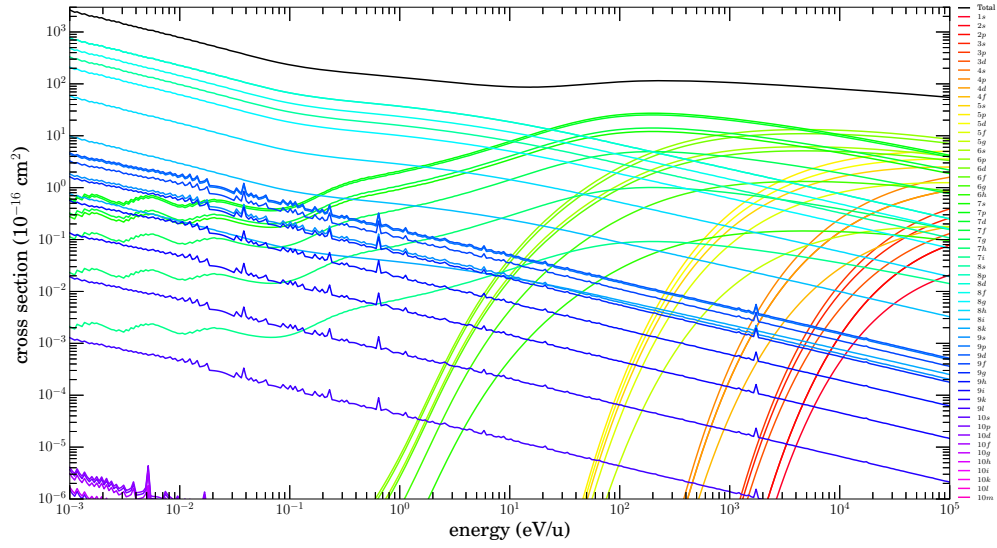
Figure 3.15 Mg^{12+}+H→Mg^{11+}+H$^+$ $n\ell$-resolved cross sections using the low-energy distribution function.
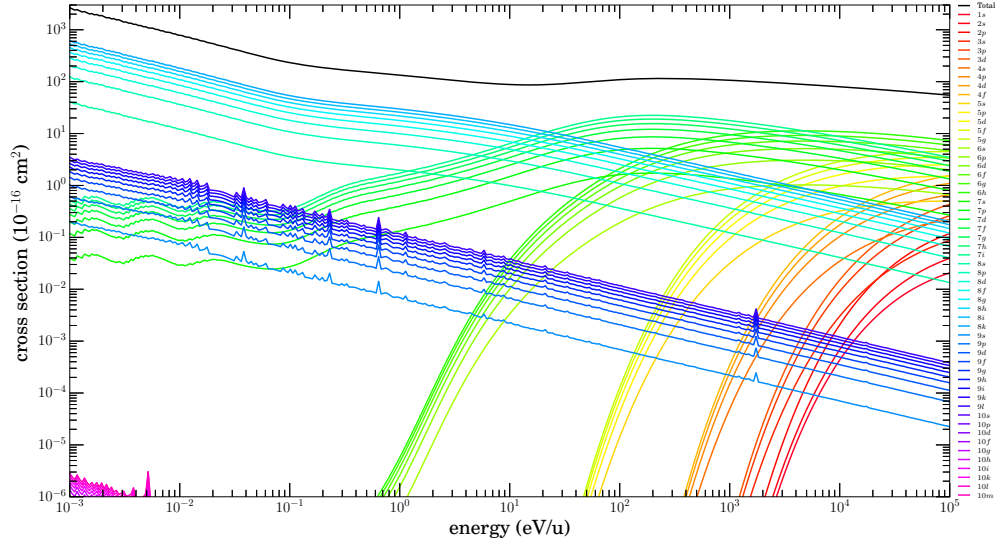
Figure 3.16 Mg^{12+}+H→Mg^{11+}+H$^+$ $n\ell$-resolved cross sections using the statistical distribution function.

3.6.2 HE

Figure 3.17 shows the n-resolved cross sections for Mg^{12+}+He→Mg^{11+}+He$^+$. The dominant channels, as shown in the figure, are listed in Table 3.10.2.
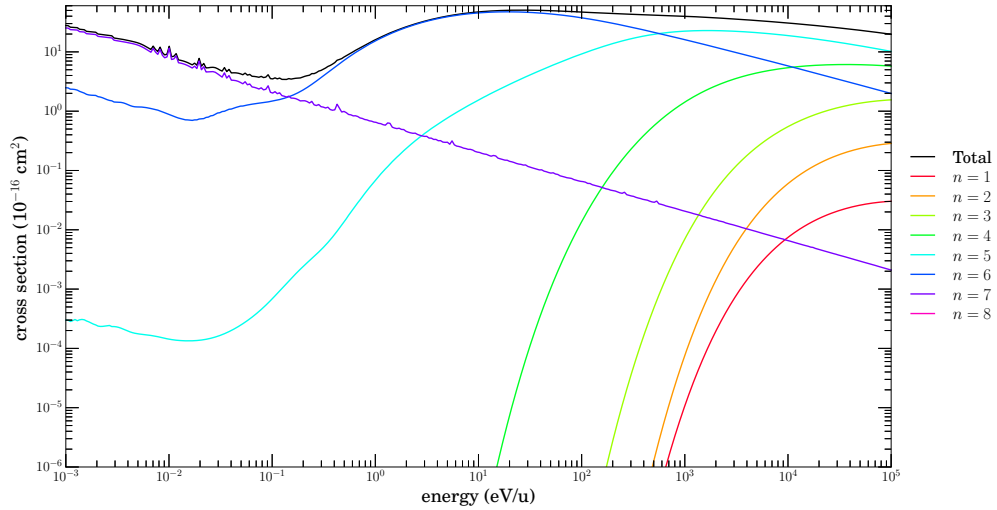
Figure 3.17 Mg^{12+}+He→Mg^{11+}+He$^+$ n-resolved cross sections.
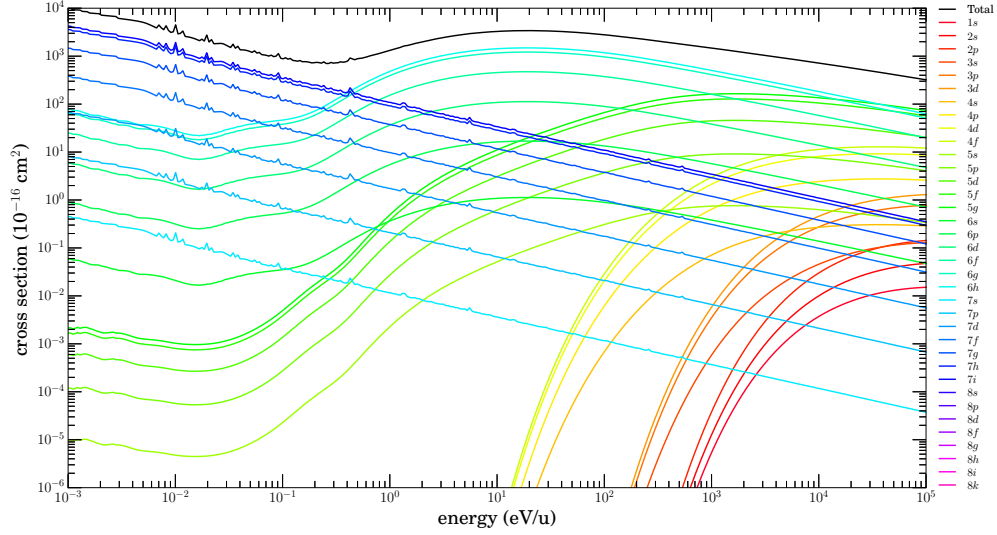
Figure 3.18 Mg^{12+}+He→Mg^{11+}+He$^+$ $n\ell$-resolved cross sections using the low-energy distribution function.
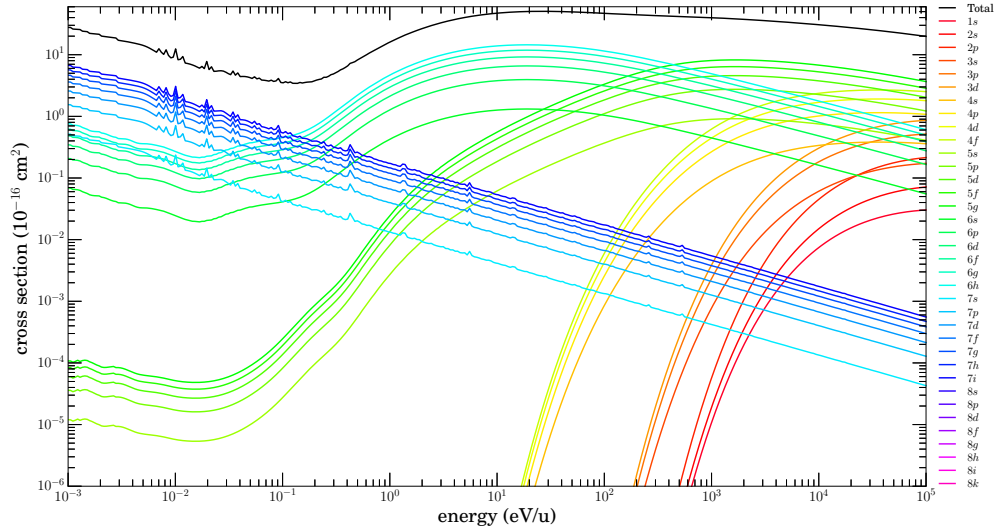
Figure 3.19 Mg^{12+}+He→Mg^{11+}+He$^+$ $n\ell$-resolved cross sections using the statisitcal distribution function.

3.7   Mg^{11+}

Figure 3.38 presents the single electron capture cross sections for the following: Mg^{11+}+H (dominant channels n=7 and n=6); Mg^{11+}+He (n=6, n=5); Mg^{10+}+H (n=7, n=6); Mg^{10+}+He

(n=5); Mg^{9+}+H (n=6); Mg^{9+}+He (n=5, n=4); Mg^{8+}+H (n=6, n=5); and Mg^{8+}+He (n=4, n=3). We are unaware of other available experimental or theoretical results for these systems.

3.7.1   H

Cross sections for Mg^{11+}+H→Mg^{10+}+H$^+$ in Figures 3.7.1, 3.7.1, and 3.7.1. There are no other experimental or theoretical data available for comparison with these results. Dominant channels are listed in Table 3.10.2.
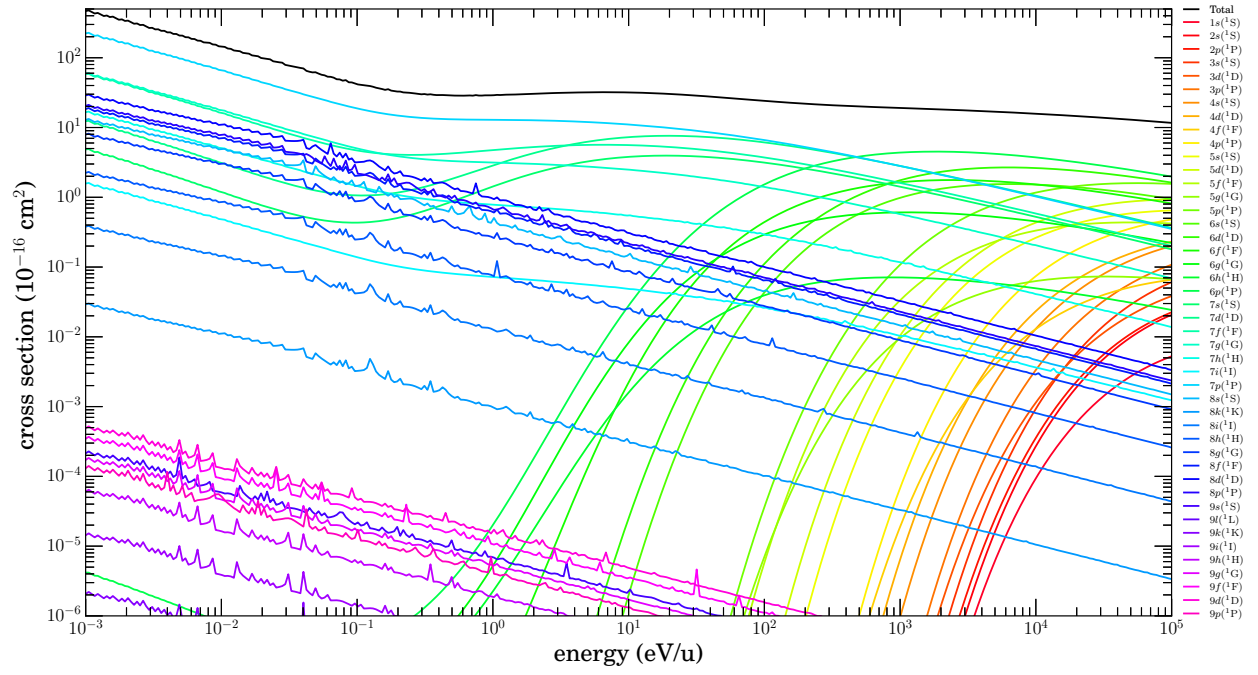
Figure 3.20 Mg^{11+}+H→Mg^{10+}+H$^+$ $n\ell$-resolved singlets cross sections.
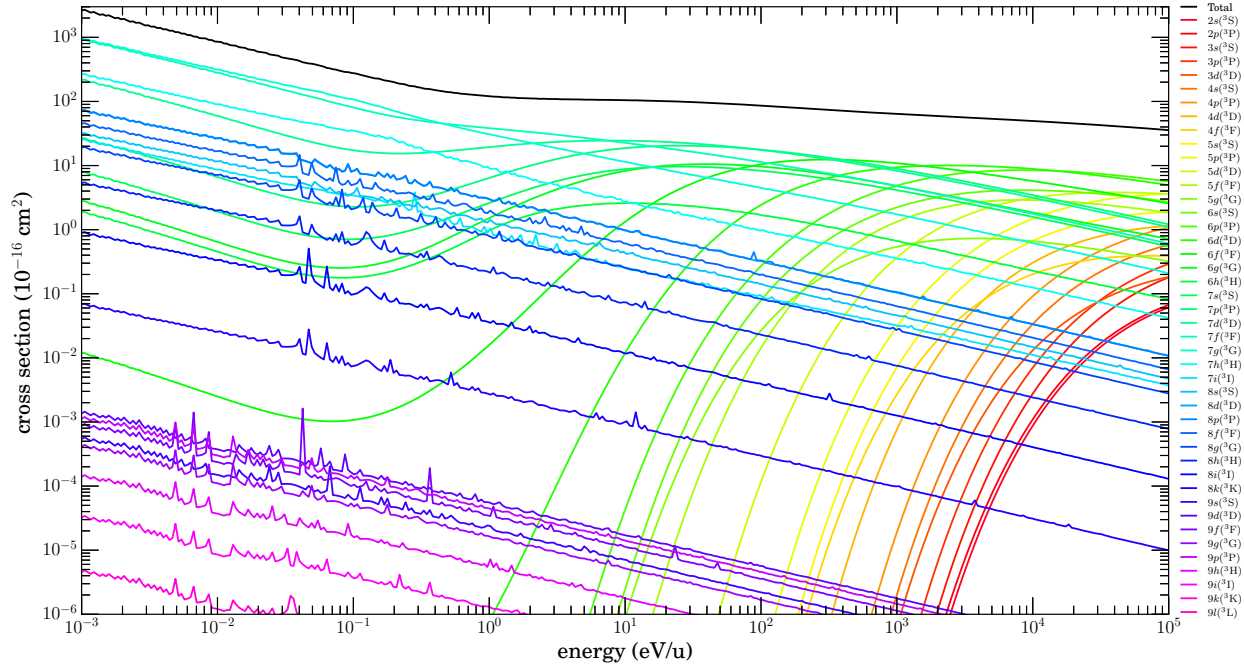
Figure 3.21 Mg^{11+}+H→Mg^{10+}+H$^+$ $n\ell$-resolved triplets cross sections.
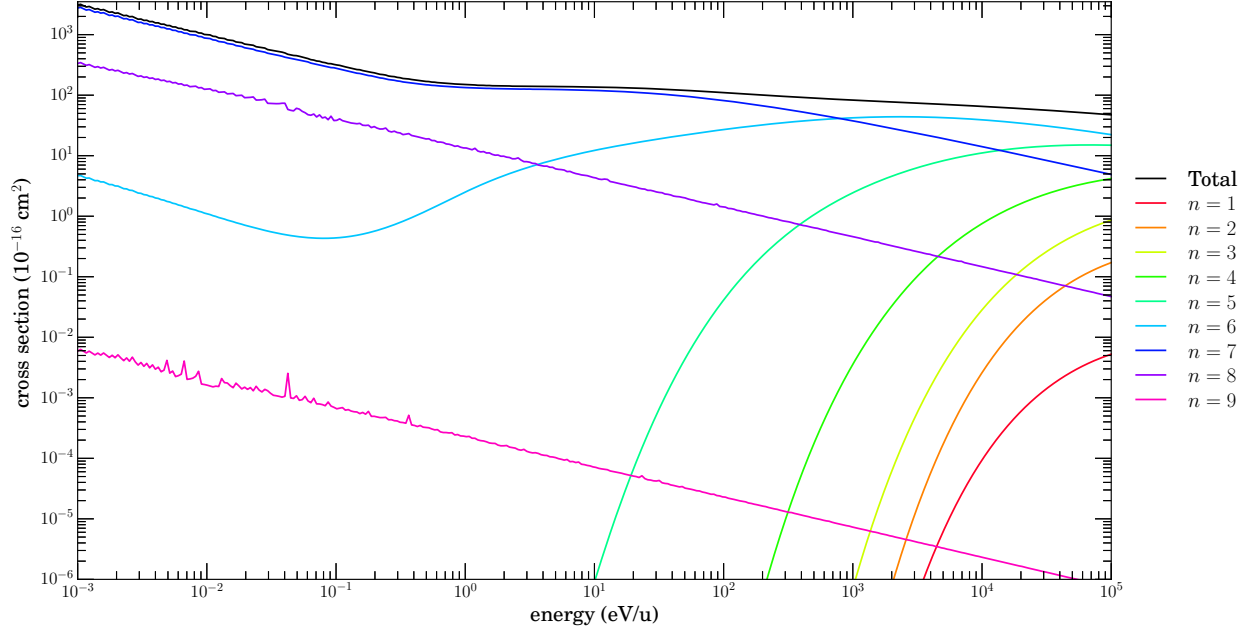
Figure 3.22 Mg^{11+}+H→Mg^{10+}+H$^+$ n-resolved cross sections (sum of singlets and triplets).

3.7.2 He

Results for $Mg^{11+}+He\rightarrow Mg^{10+}+He^+$ are shown in Figures 3.7.2 and 3.7.2. Dominant channels are listed in Table 3.10.2. Again, with this system, no previously publish results are available.
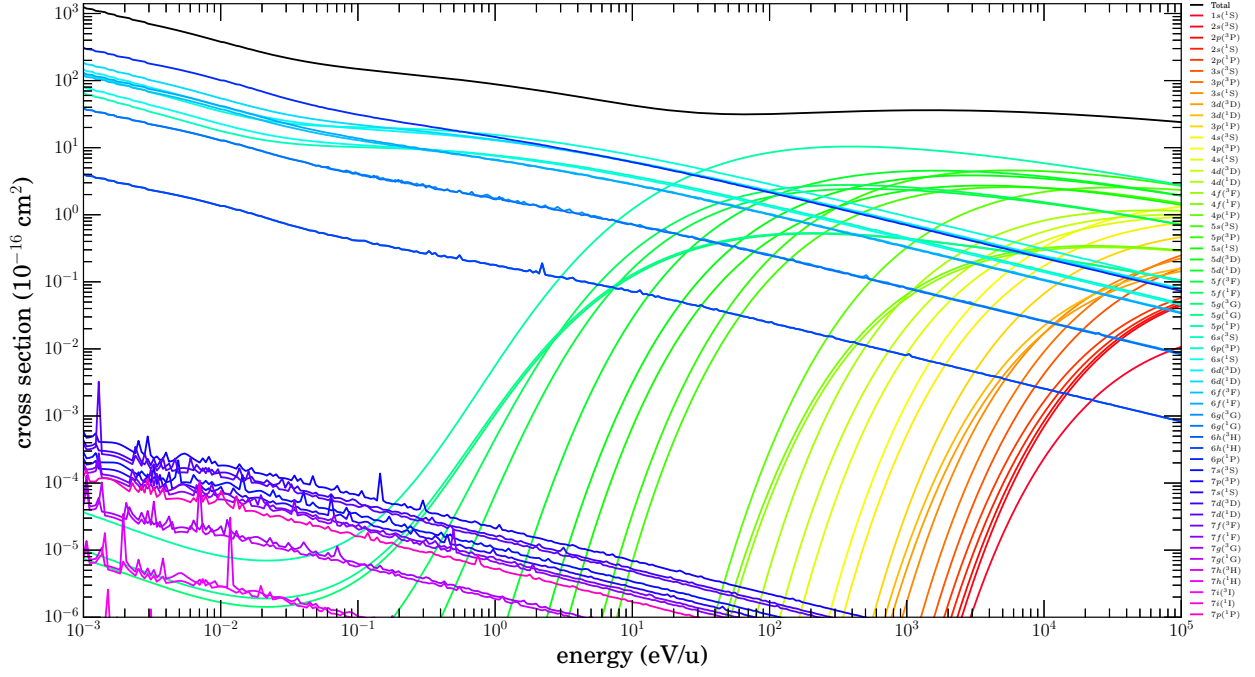
Figure 3.23 $Mg^{11+}+He\rightarrow Mg^{10+}+He^+$ $n\ell$-resolved cross sections.
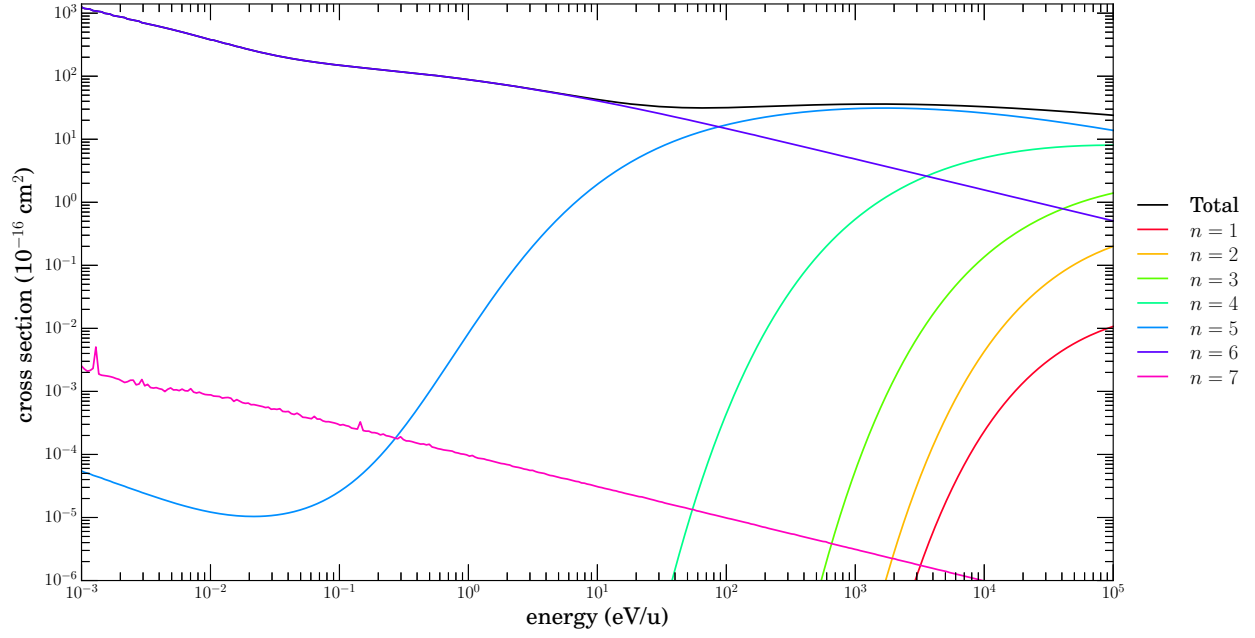
Figure 3.24 $Mg^{11+}+He \rightarrow Mg^{10+}+He^+$ n-resolved cross sections.

3.8 Mg^{10+}

3.8.1 H
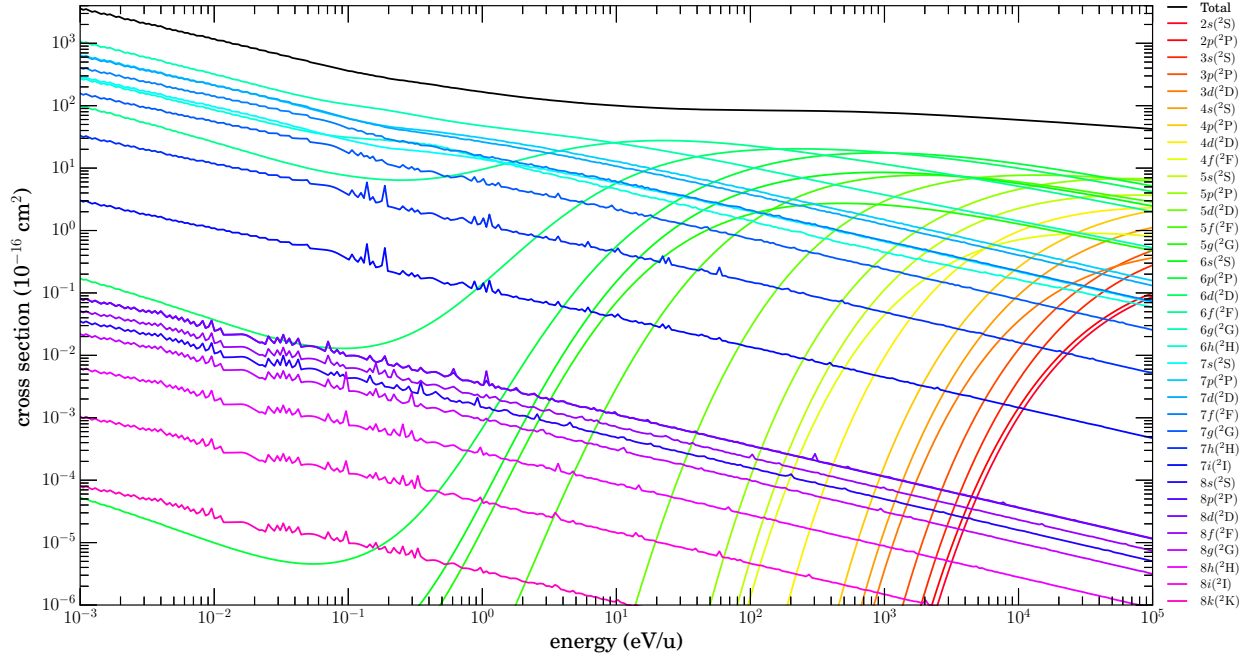
Figure 3.25 Mg^{10+}+H→Mg^{9+}+H$^+$ $n\ell$-resolved cross sections.
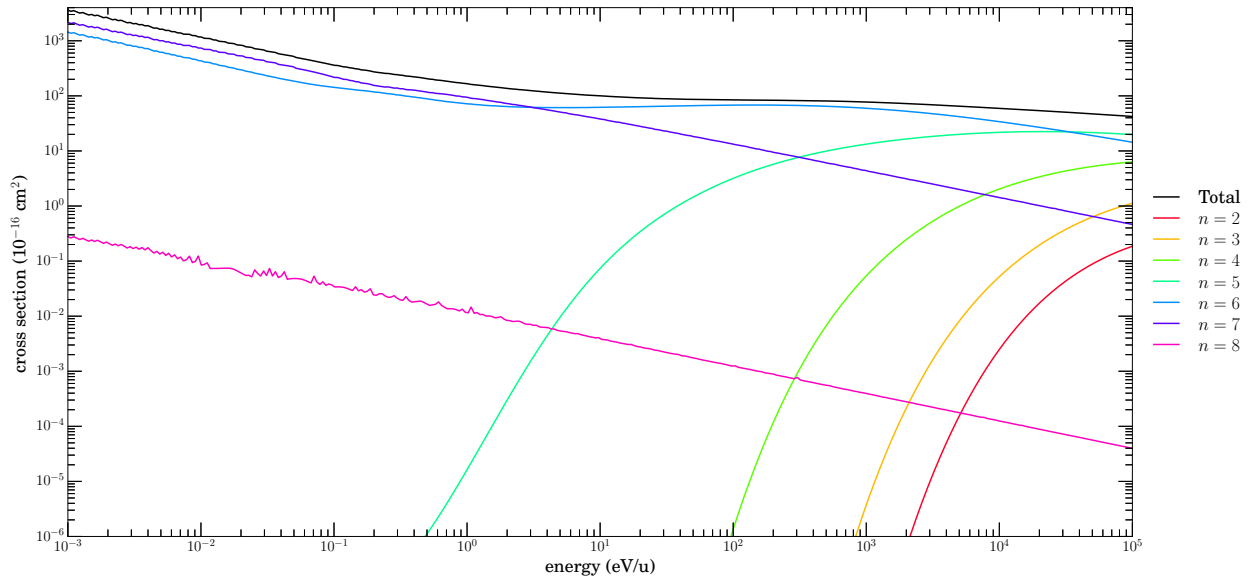
Figure 3.26 Mg^{10+}+H→Mg^{9+}+H$^+$ n-resolved cross sections.

28

3.8.2 He
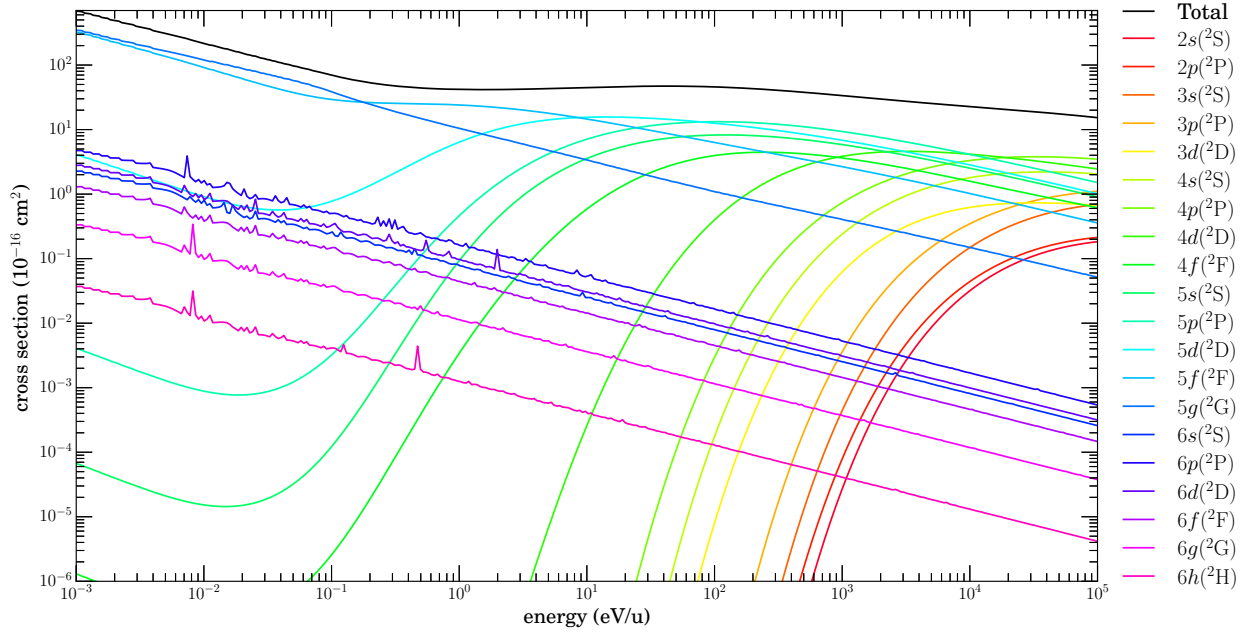
Figure 3.27 Mg^{10+}+He→Mg^{9+}+He$^+$ $n\ell$-resolved cross sections.
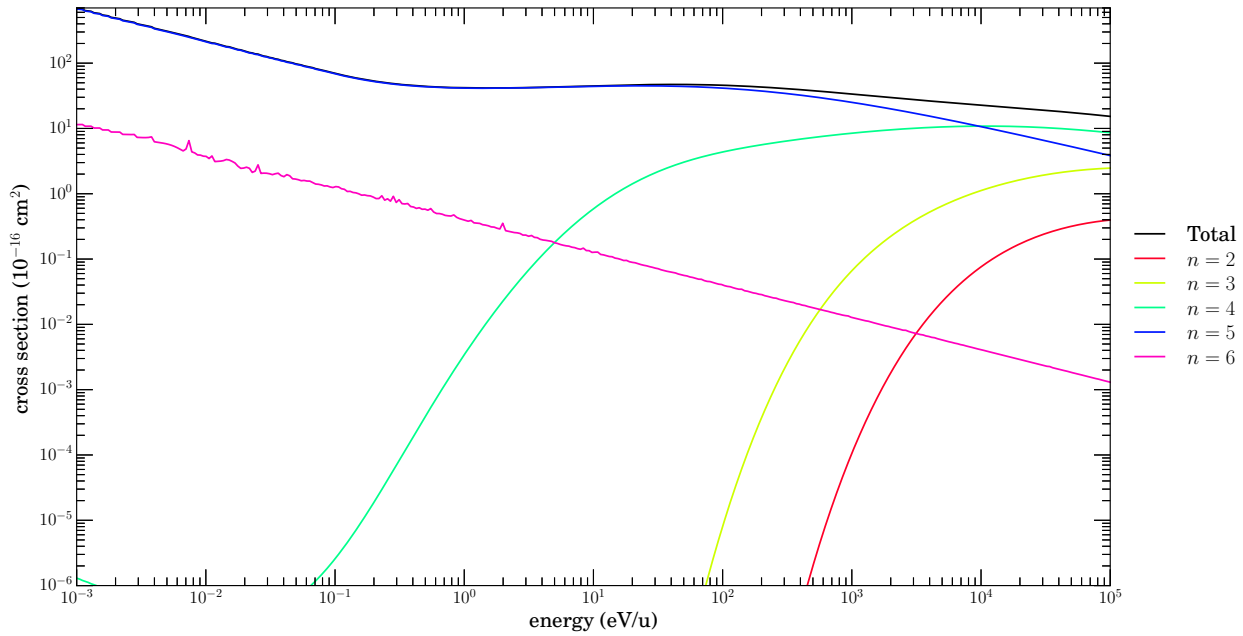
Figure 3.28 Mg^{10+}+He→Mg^{9+}+He$^+$ n-resolved cross sections.

3.9 Mg^{9+}

3.9.1 H
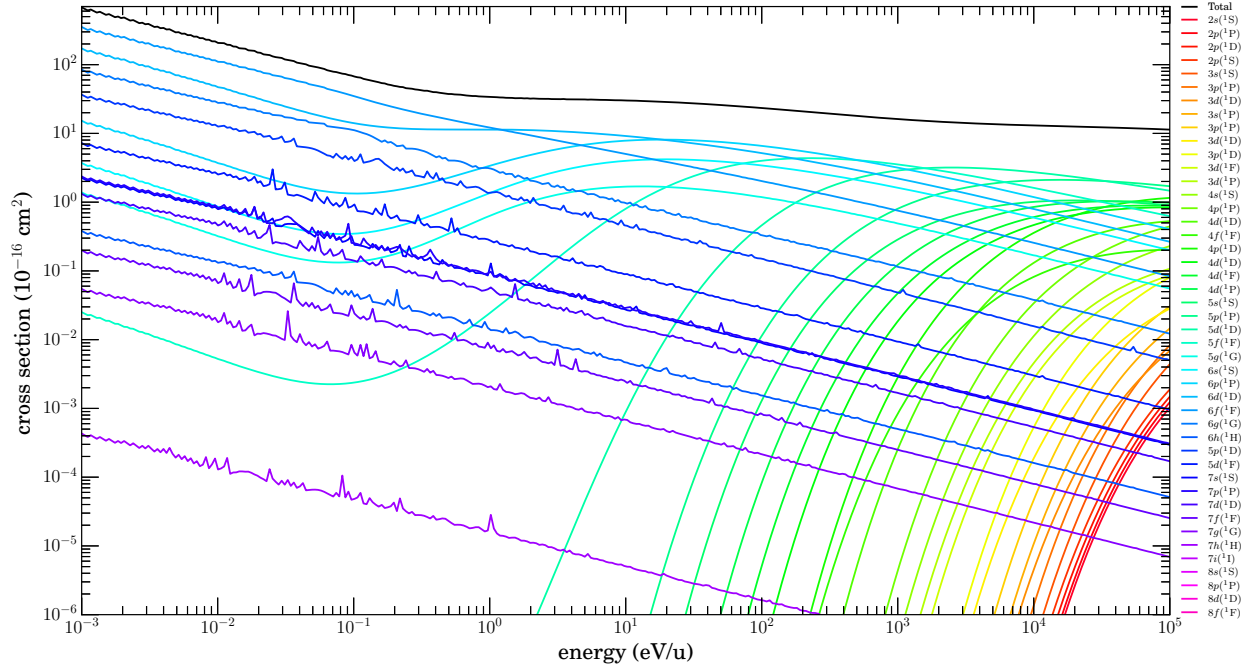
Figure 3.29 Mg^{9+}+H→Mg^{8+}+H$^+$ $n\ell$-resolved singlets cross sections.
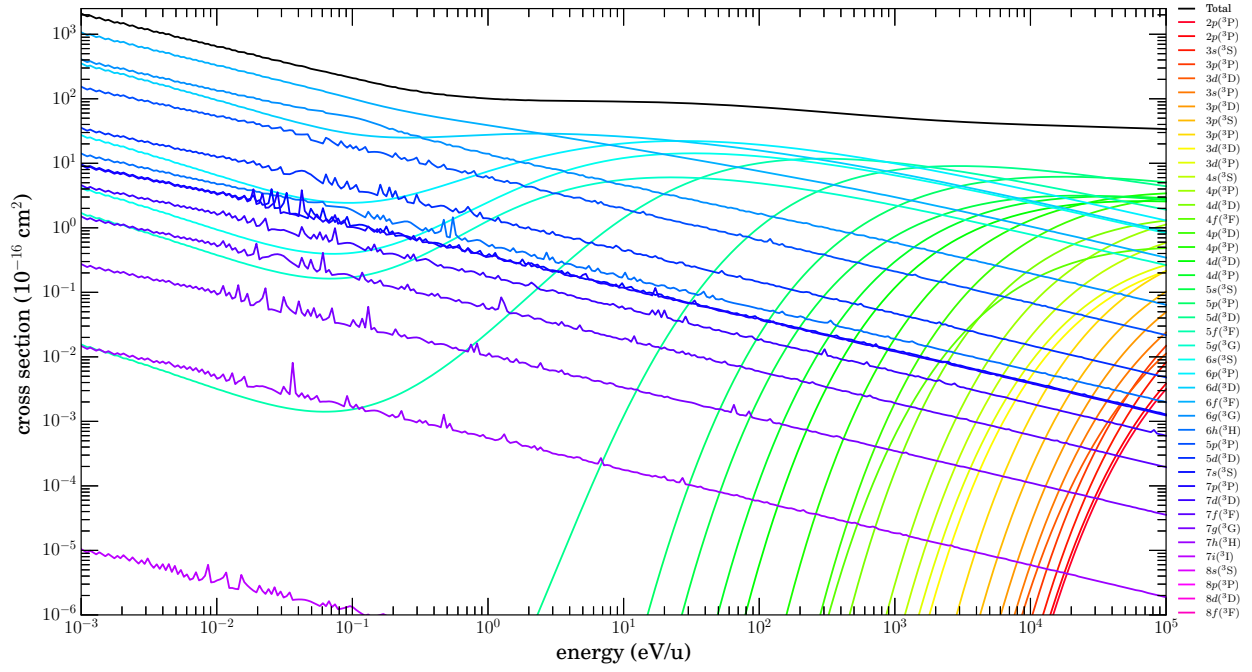
Figure 3.30 $Mg^{9+}+H \rightarrow Mg^{8+}+H^+$ $n\ell$-resolved triplets cross sections.
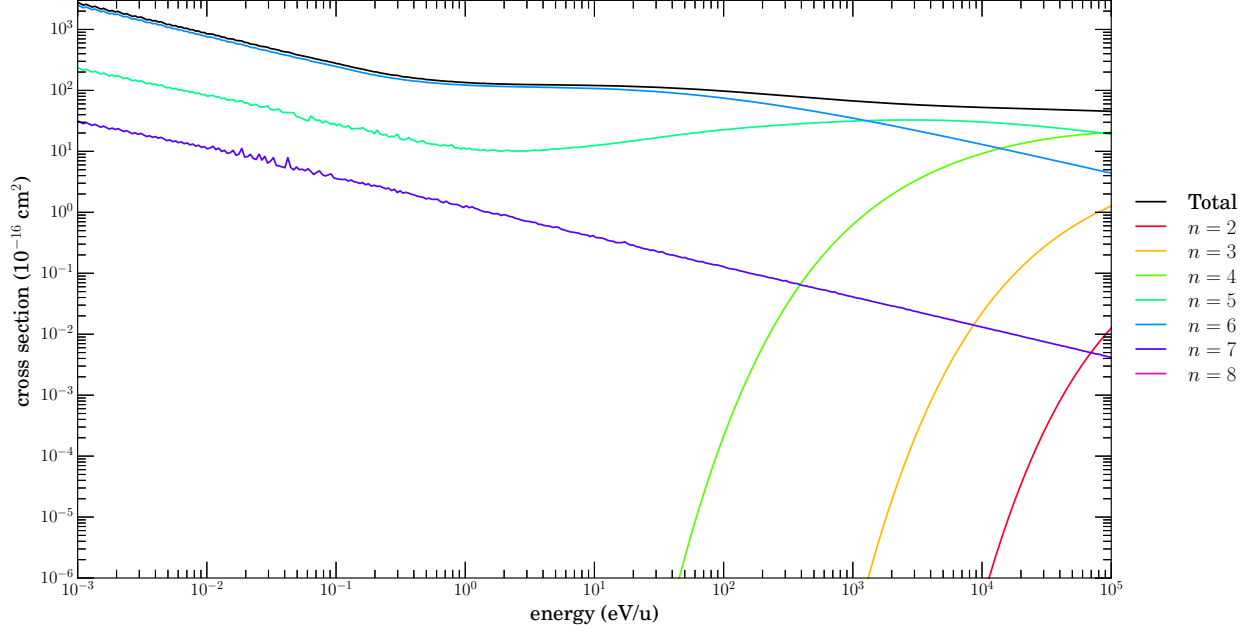
Figure 3.31 $Mg^{9+}+H \rightarrow Mg^{8+}+H^+$ n-resolved cross sections.
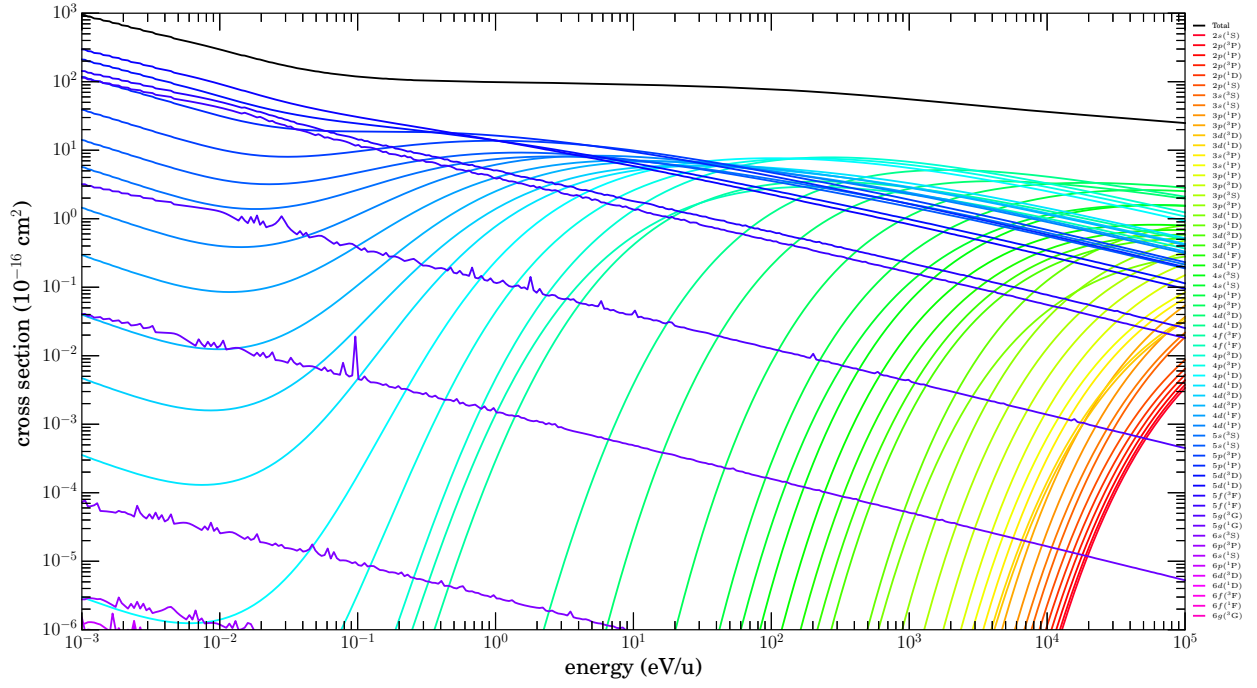
Figure 3.32 Mg^{9+}+He→Mg^{8+}+He$^+$ $n\ell$-resolved cross sections.
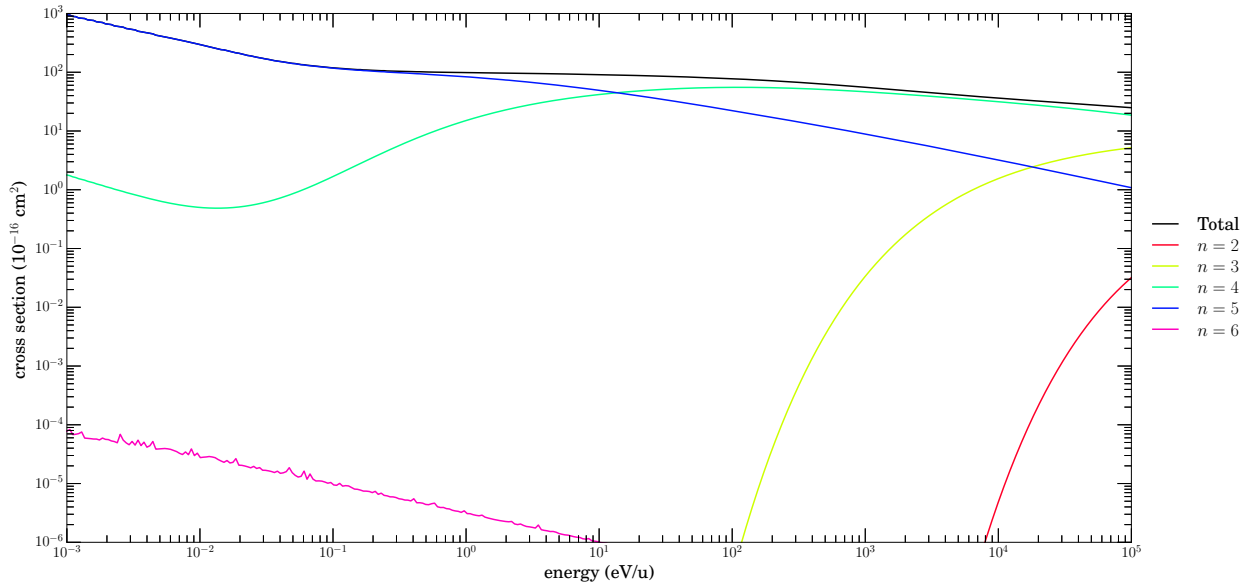
Figure 3.33 Mg^{9+}+He→Mg^{8+}+He$^+$ n-resolved cross sections.

3.10 Mg^{8+}

3.10.1 H
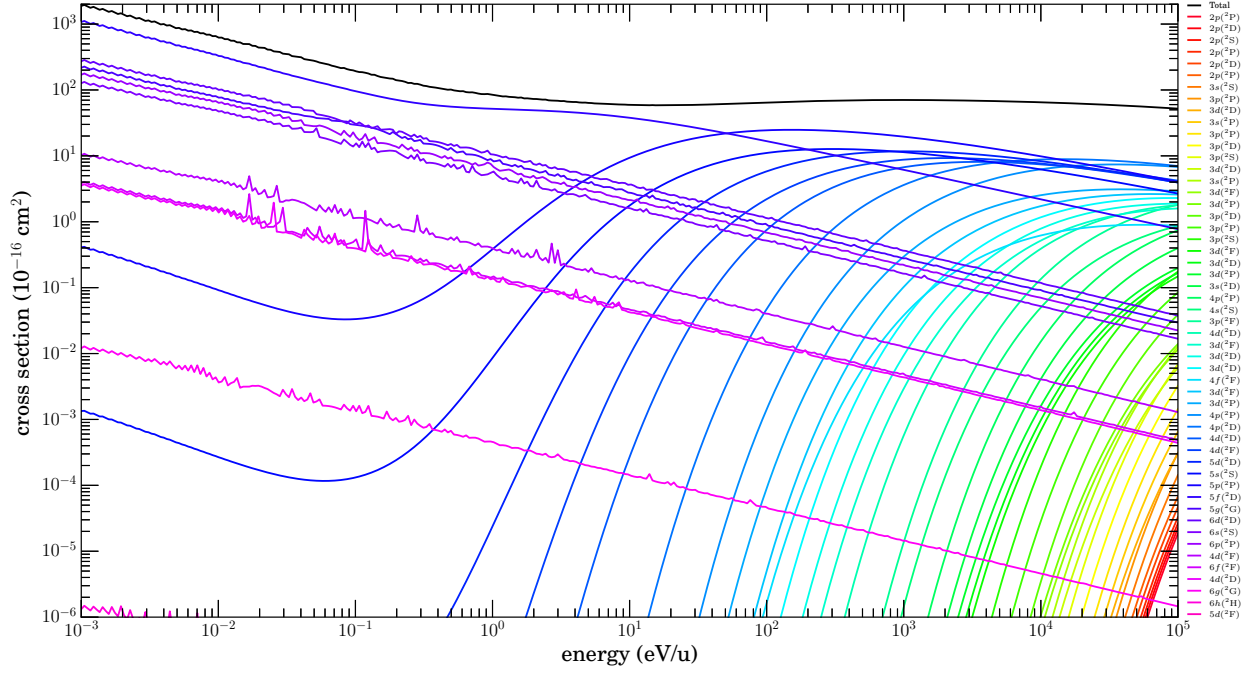
Figure 3.34 Mg^{8+}+H→Mg^{7+}+H$^+$ $n\ell$-resolved cross sections.
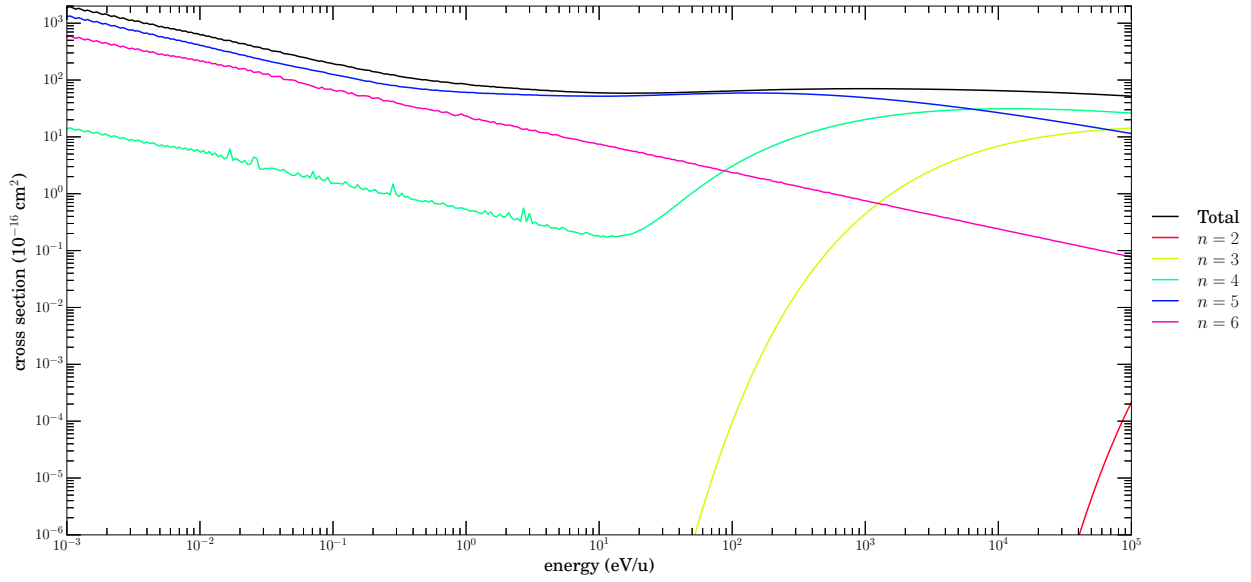
Figure 3.35 Mg^{8+}+H→Mg^{7+}+H$^+$ n-resolved cross sections.
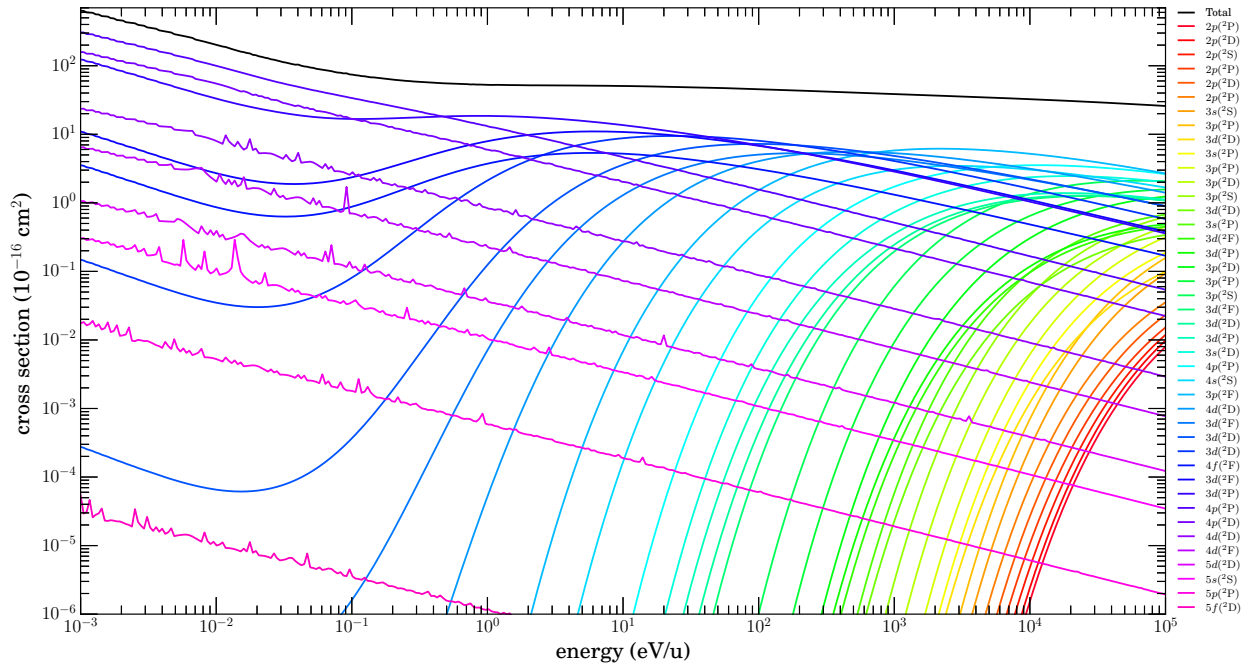
Figure 3.36 Mg^{8+}+He→Mg^{7+}+He$^+$ $n\ell$-resolved cross sections.
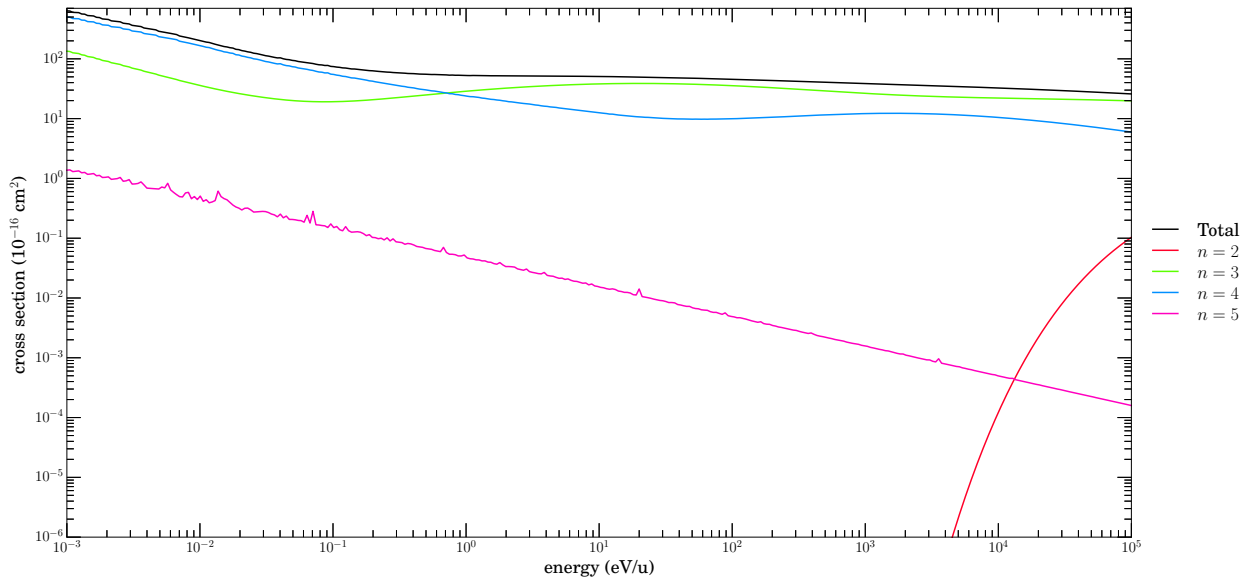
Figure 3.37 Mg^{8+}+He→Mg^{7+}+He$^+$ n-resolved cross sections.

Table 3.1. $\mathrm{Mg}^{(12-8)+}$ Dominant Channels

System	Channel	eV/u
$\mathrm{Mg}^{12+}+\mathrm{H}\rightarrow\mathrm{Mg}^{11+}+\mathrm{H}^+$	n=8	$\lesssim$2.5e1
	n=7	2.5e1–7.4e3
	n=6	$\gtrsim$7.4e3
$\mathrm{Mg}^{12+}+\mathrm{He}\rightarrow\mathrm{Mg}^{11+}+\mathrm{He}^+$	n=7	$\lesssim$1.5e-1
	n=6	1.5e-1–5.6e2
	n=5	$\gtrsim$5.6e2
$\mathrm{Mg}^{11+}+\mathrm{H}\rightarrow\mathrm{Mg}^{10+}+\mathrm{H}^+$	n=7	$\lesssim$7.9e2
	n=6	$\gtrsim$7.9e2
$\mathrm{Mg}^{11+}+\mathrm{He}\rightarrow\mathrm{Mg}^{10+}+\mathrm{He}^+$	n=6	$\lesssim$8.7e1
	n=5	$\gtrsim$8.7e1
$\mathrm{Mg}^{10+}+\mathrm{H}\rightarrow\mathrm{Mg}^{9+}+\mathrm{H}^+$	n=7	$\lesssim$3.1e0
	n=6	3.1e0–3.3e4
	n=5	$\gtrsim$3.3e4
$\mathrm{Mg}^{10+}+\mathrm{He}\rightarrow\mathrm{Mg}^{9+}+\mathrm{He}^+$	n=5	$\lesssim$9.6e3
	n=4	$\gtrsim$9.6e3
$\mathrm{Mg}^{9+}+\mathrm{H}\rightarrow\mathrm{Mg}^{8+}+\mathrm{H}^+$	n=6	$\lesssim$1.3e3
	n=5	1.3e3–8.4e4
	n=4	$\gtrsim$8.4e4
$\mathrm{Mg}^{9+}+\mathrm{He}\rightarrow\mathrm{Mg}^{8+}+\mathrm{He}^+$	n=5	$\lesssim$1.4e1
	n=4	$\gtrsim$1.4e1
$\mathrm{Mg}^{8+}+\mathrm{H}\rightarrow\mathrm{Mg}^{7+}+\mathrm{H}^+$	n=5	$\lesssim$6.5e3
	n=4	$\gtrsim$6.5e3
$\mathrm{Mg}^{8+}+\mathrm{He}\rightarrow\mathrm{Mg}^{7+}+\mathrm{He}^+$	n=4	$\lesssim$7.1e-1
	n=3	$\gtrsim$7.1e-1
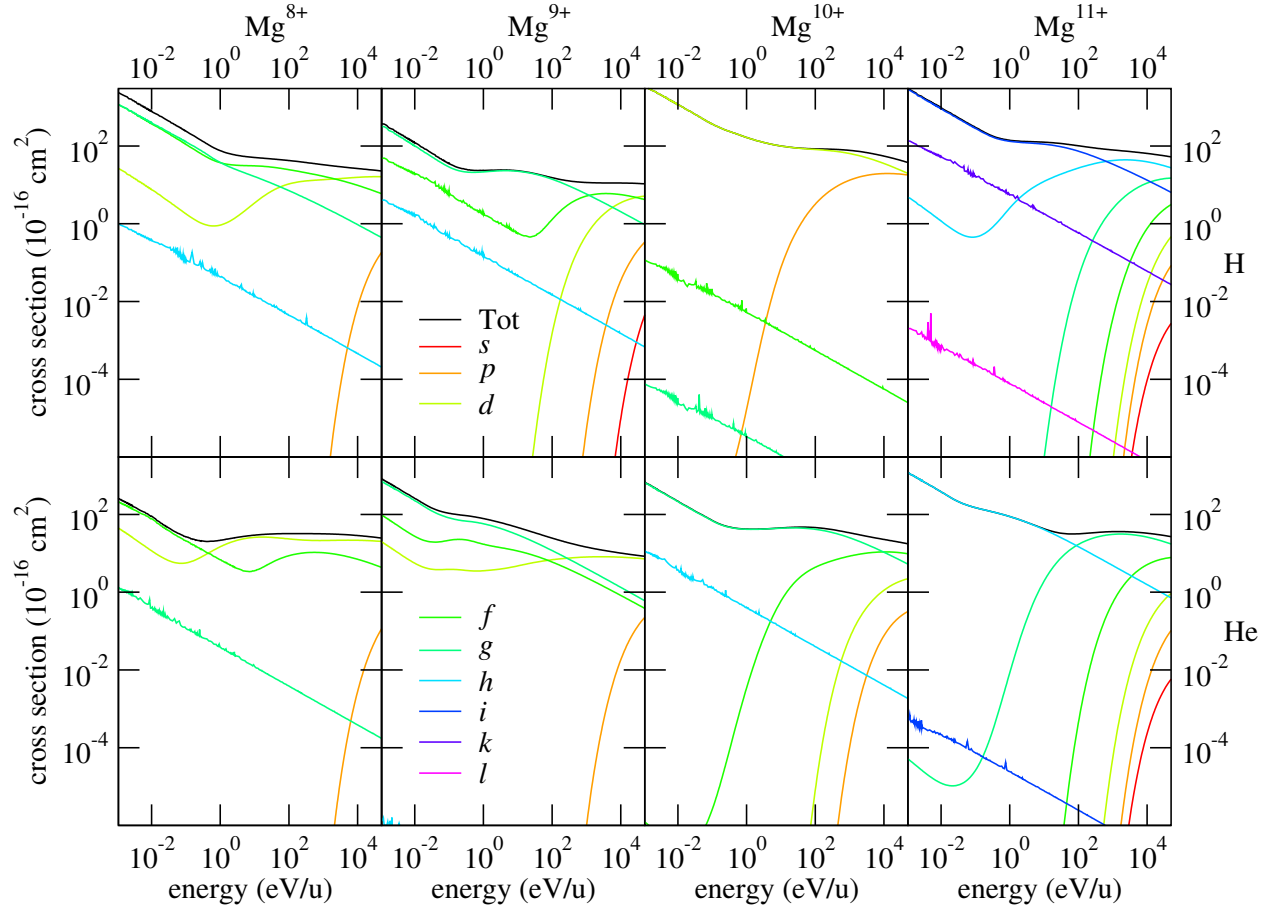
Figure 3.38 MCLZ single electron capture cross sections, n-resolved, for Mg^{q+} ions, q=8–11, colliding with hydrogen (H) and helium (He) atoms.

FE$^{(8-9)+}$ WITH H, H$_2$, HE, H$_2$O, CO, CO$_2$, AND N$_2$ USING MCLZ

[1]

4.1 METHODS

4.1.1 ESTIMATION OF MISSING ENERGIES FOR FE^{7+}

When the Landau-Zener method (Butler and Dalgarno 1980; Janev et al. 1983; Lyons et al. 2017) is used to calculate cross sections from atom-ion collisions resulting in single electron capture (SEC) charge exchange, it is necessary to begin with excitation energies of the ion states for which cross sections are desired (Lyons et al. 2017). These energies may be obtained from NIST (Kramida et al. 2018) and other sources. NIST provides the energies for various states (given by their electron configurations) as shown in Table 4.4. However, for many states the highly-excited Rydberg levels are unknown. Therefore they can be calculated or estimated using a variety of methods.

We are not concerned with quartets, only doublets. Also, we are attempting to estimate missing energies only for singly-excited states (i.e., only the valence electron is excited). We want to use the energies for the singly-excited states to estimate the energies of those singly-excited states which are not available. That leaves the following data available, as shown in Table 4.4, which we will use to estimate the missing energies using a form of the Quantum Defect relation (Connerade 1998; Lyons et al. 2017; Mullen et al. 2016)

$$E(n) = E_0(1 - \frac{1}{(n - \mu)^2}) \tag{4.1}$$

[1]Lyons, David A., and Stancil, Phillip C., 2019. To be submitted to *The Astrophysical Journal.*
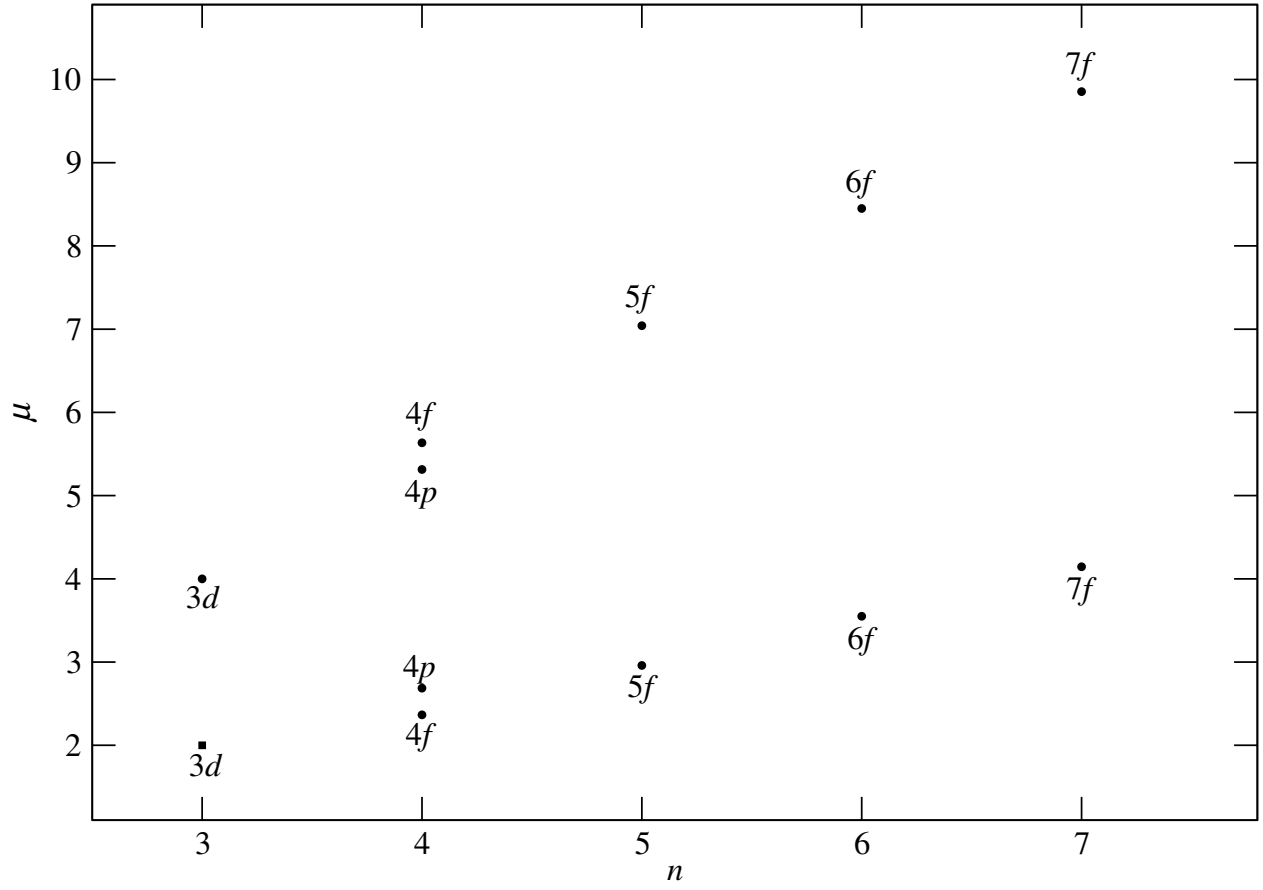
Figure 4.1 μ vs. n for the excitation energies provided by NIST for singly-excited states of Fe^{7+}.

Solving for μ gives

$$\mu = n \pm \sqrt{\frac{1}{1 - \frac{E(n)}{E_0}}} \tag{4.2}$$
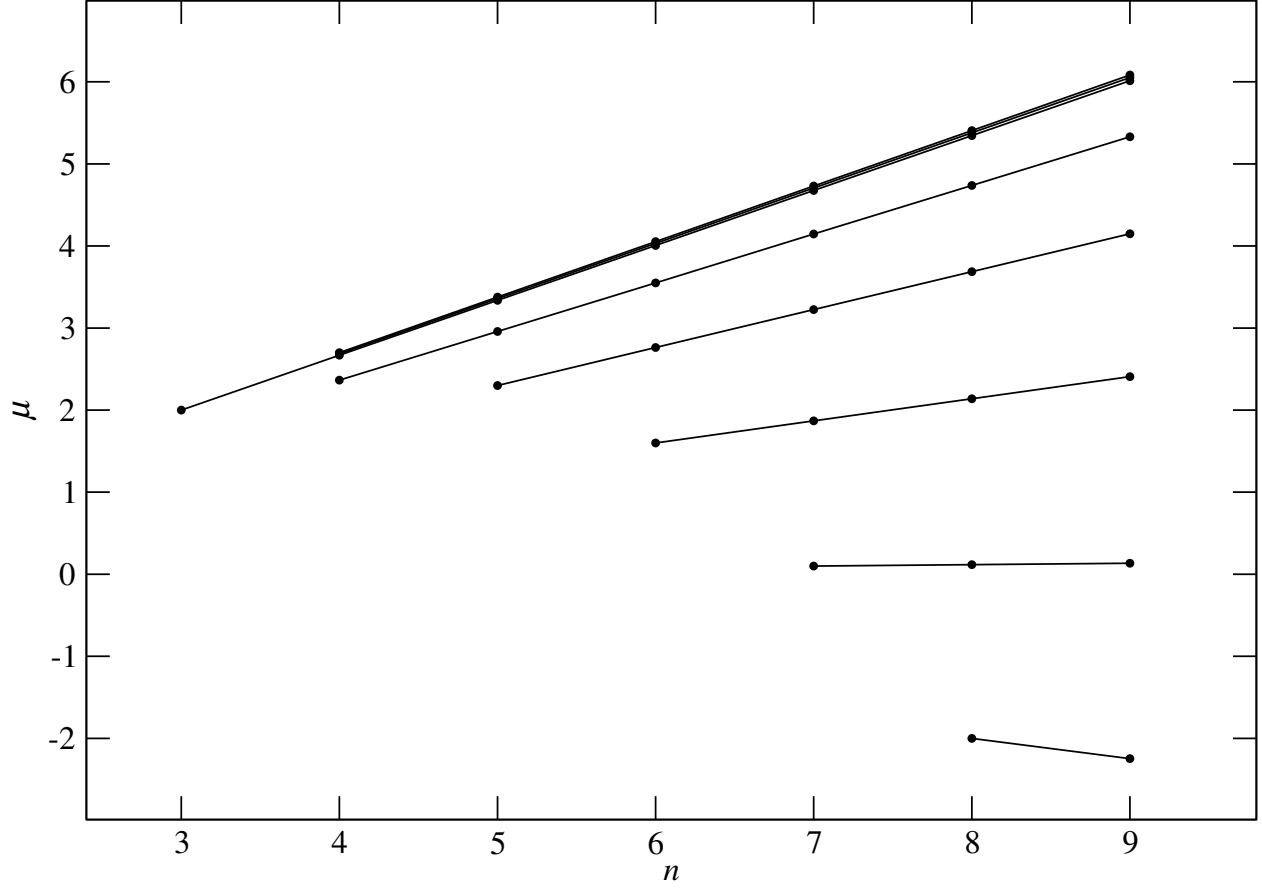
Figure 4.2 μ vs. n for the excitation energies provided by NIST, and those estimated, for singly-excited states of Fe^{7+}.

Equation 4.2 shows that there can be two values for μ, which are called μ_+ and μ_-. Using the term energies in Table 4.4, the values of μ_+ and μ_- are plotted and shown in Figure 4.1, where the linearity of the μ_+ and μ_- values for $\ell=3$ (f states) appear to converge at or near the origin. It is assumed that for all other values of ℓ, the values of μ_+ and μ_- are also linear and converge at the same point. Thus, the values of μ_+ and μ_- are calculated for all n where $\ell=1$, $\ell=2$, and $\ell=3$. The results of these calculations are shown in Figure 4.2. Since there is no data available for states where $\ell=4$ and above, the values of μ are estimated graphically and adjusted until the resulting term energies (obtained with Equation 4.1) fit as expected with the rest of the data. The estimated term energies, along with those provided by NIST, are shown in Table 4.4.

4.1.2 Estimation of Missing Energies for Fe^{8+}

Fe^{8+} has even fewer energies available which can be used to predict the missing values. Furthermore, this ion has a number of ambiguous states (i.e., it is unclear whether these ambiguous states are singlets or triplets). However, the same assumptions are used for Fe^{8+} as those used for Fe^{7+}: the μ values are linear in n for a given ℓ, and they pass through the origin for $n=0$. For Fe^{8+}, singlets and triplets are calculated separately. For the ambiguous states, assumptions are made whether these are included in the calculations for singlets or triplets. These assumptions are based on the electron configuration and term. For this ion, Wigner-Witmer rules are applied, and the resulting molecular channels are further divided in to Σ and Π states. As with singlets and triplets, these are calculated separately. For these states, there are also degeneracy factors which are needed in the cross section calculations, as shown in Table 4.4. The available energies are sourced from the NIST database, and are shown in Table 4. Based on those term energies of the singly-excited states, the μ values are adjusted such that the resulting energy falls into an expected range, based on the other energies given. For example, a singly-exited state should have a lower energy than a similar state where the core is excited. An example would be as follows: the singly-excited state $3s^23p^54p(^1P^\circ)$ should have a lower energy than that for the core-excited state $3s3p^64p(^1P^\circ)$. The value of μ is adjusted in increments of 0.1 until the term energy falls into the appropriate range. In some cases, increments of μ are adjusted by 0.01 or even 0.001 until the energy for that state falls into a reasonable range. After μ is estimated for $3s^23p^54p(^1P^\circ)$, then μ is found for $3s^23p^55p(^1P^\circ)$, $3s^23p^56p(^1P^\circ)$, and so on, using the linear assumption. Next, it is assumed that $3s^23p^54s(^1S^\circ)$ will have a lower energy than $3s^23p^54p(^1P^\circ)$. So a similar adjustment of μ is made until the energy is satisfactorily estimated. Then the rest of the μ values for $5s$, $6s$, etc. can be calculated. The process continues for the next ℓ quantum number, d, then f, and so on. The resulting estimated and given energies are shown in Table 5 (singlets) and Table 6 (triplets).

4.2   Fe^{9+}
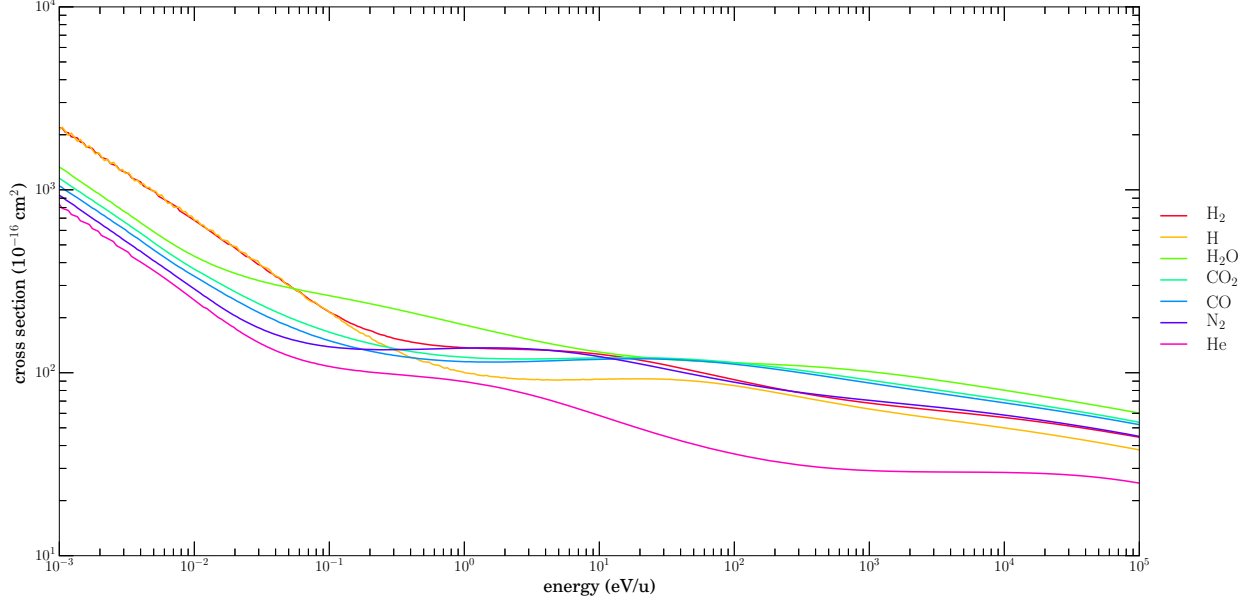
Figure 4.3 Fe^{9+}+Y→Fe^{8+}+Y^+ SEC total MCLZ cross sections.

For this system, singlet and triplet cross sections are calculated separately. Furthermore, separate calculations are performed for Σ and Π states for the singlets and triplets. Thus, there are 4 separate calculations performed for Fe^{9+}+H→Fe^{8+}+H$^+$, identified by $^1\Sigma$, $^1\Pi$, $^3\Sigma$ and $^3\Pi$. These four results are summed into a final result, shown in Figure 10.
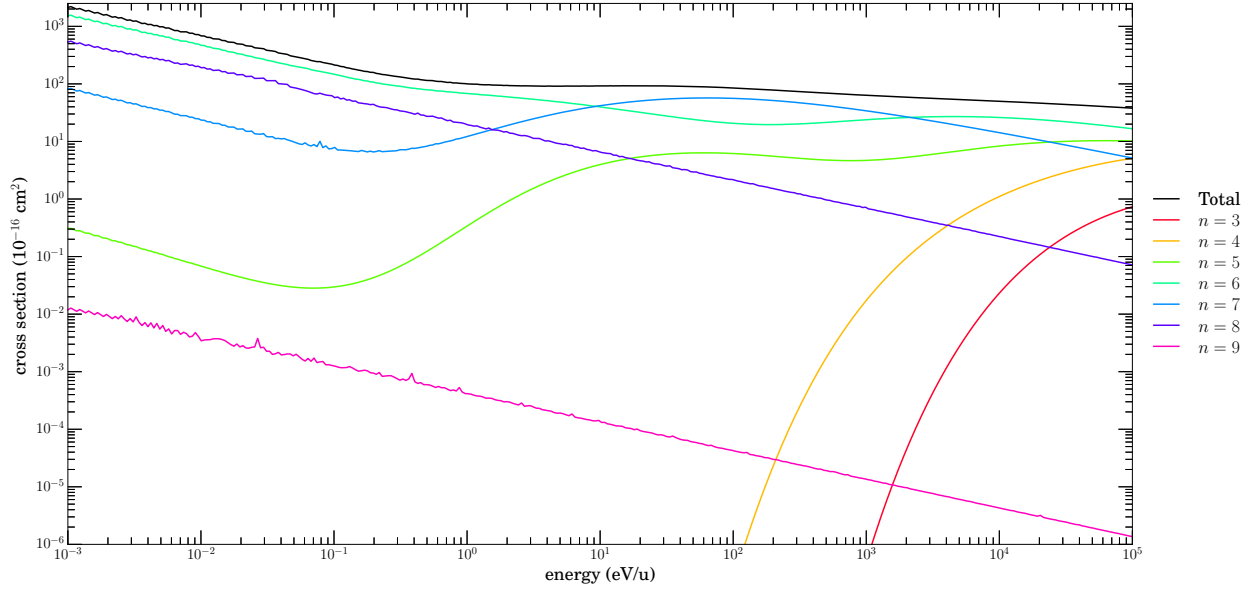
Figure 4.4 $Fe^{9+}+H \rightarrow Fe^{8+}+H^+$ MCLZ n-resolved cross sections.

For systems where the neutral atom is not hydrogen-like, it is necessary to perform separate calculations for Σ and Π states, according to Wigner-Witmer rules. These Σ and Π calculations are combined into single cross-section results for each system, shown in Figures 4.3–4.10. Results are included from Simcic et al. (2010a) and Simcic et al. (2010b) where available, which confirm the accuracy of the MCLZ method used here.
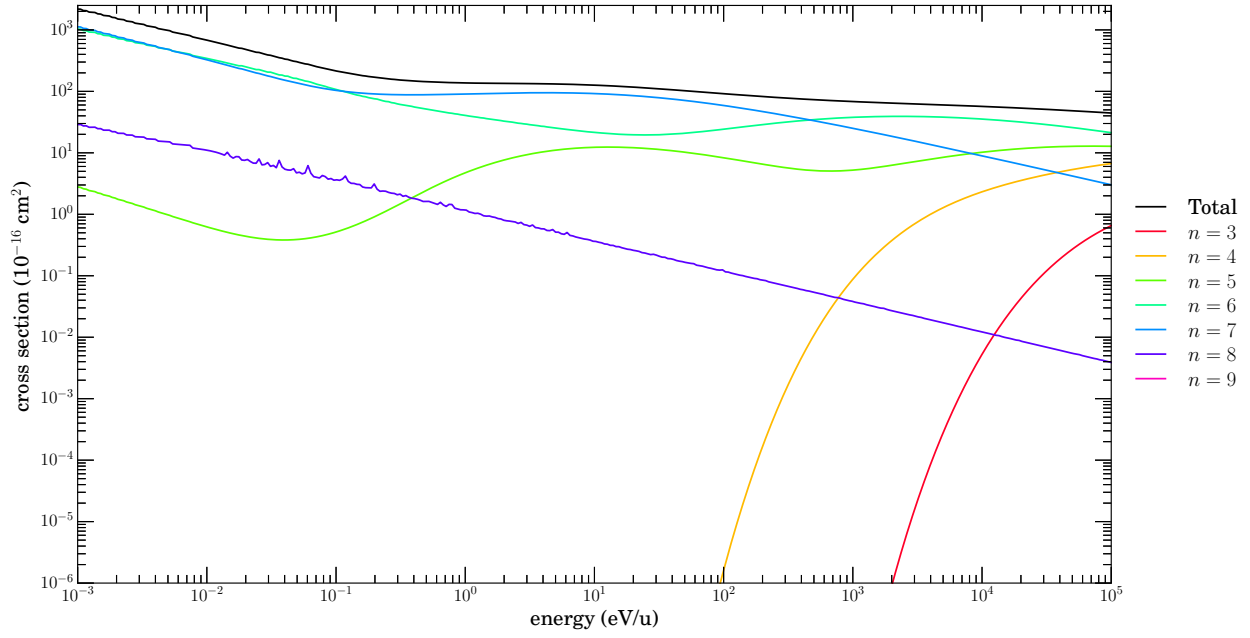
Figure 4.5 $Fe^{9+}+H_2 \rightarrow Fe^{8+}+H_2^+$ MCLZ n-resolved cross sections.
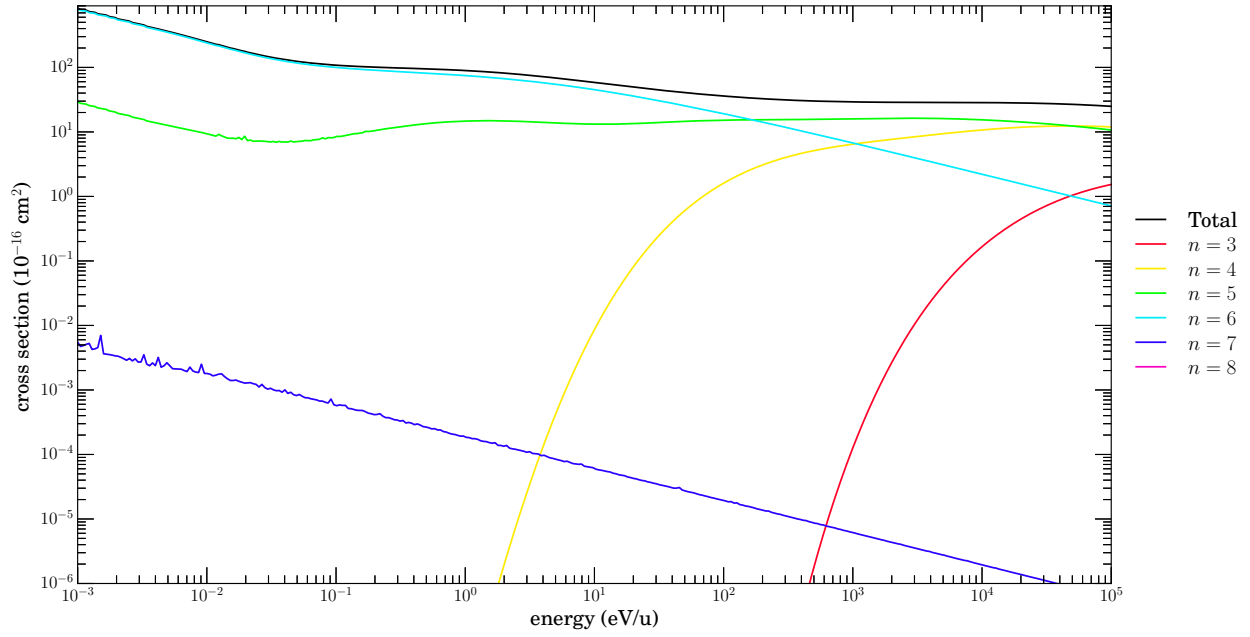
Figure 4.6 $Fe^{9+}+He \rightarrow Fe^{8+}+He^+$ MCLZ n-resolved cross sections.
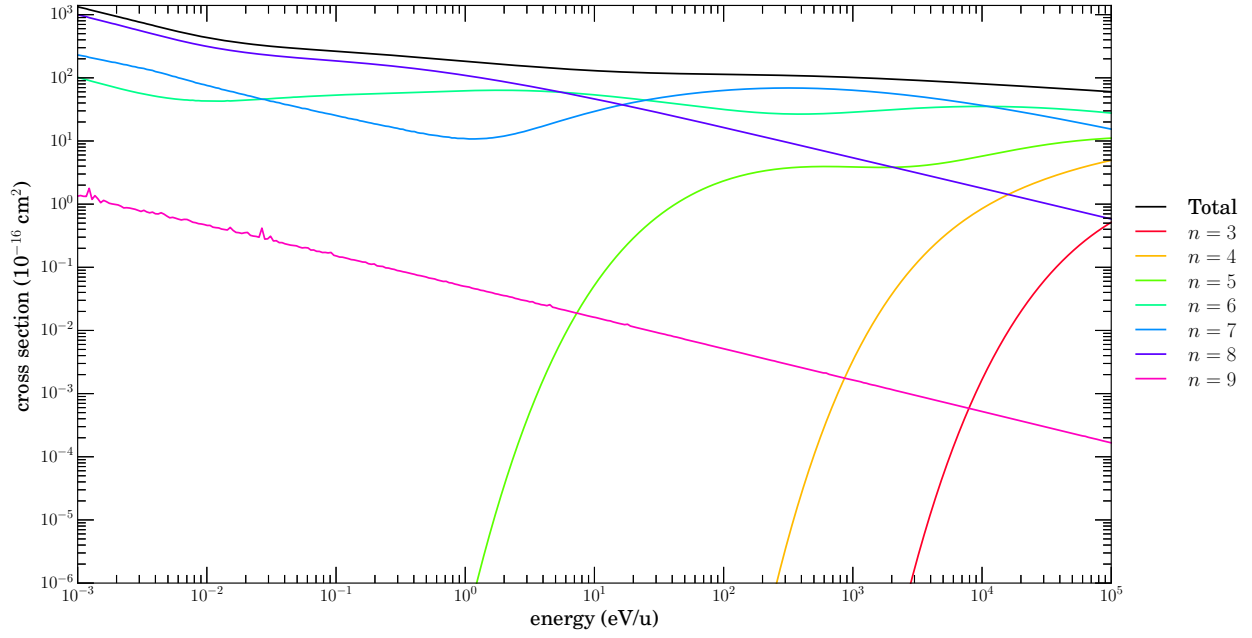
Figure 4.7 $Fe^{9+}+H_2O \rightarrow Fe^{8+}+H_2O^+$ MCLZ n-resolved cross sections.
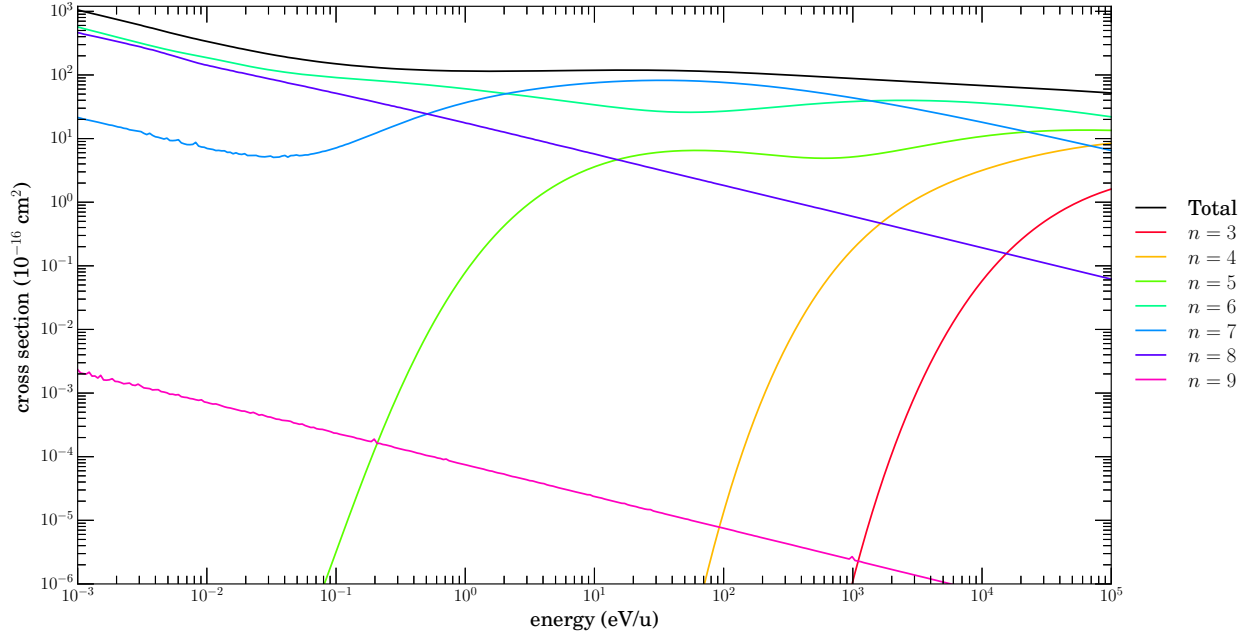
Figure 4.8 $Fe^{9+}+CO \rightarrow Fe^{8+}+CO^+$ MCLZ n-resolved cross sections.
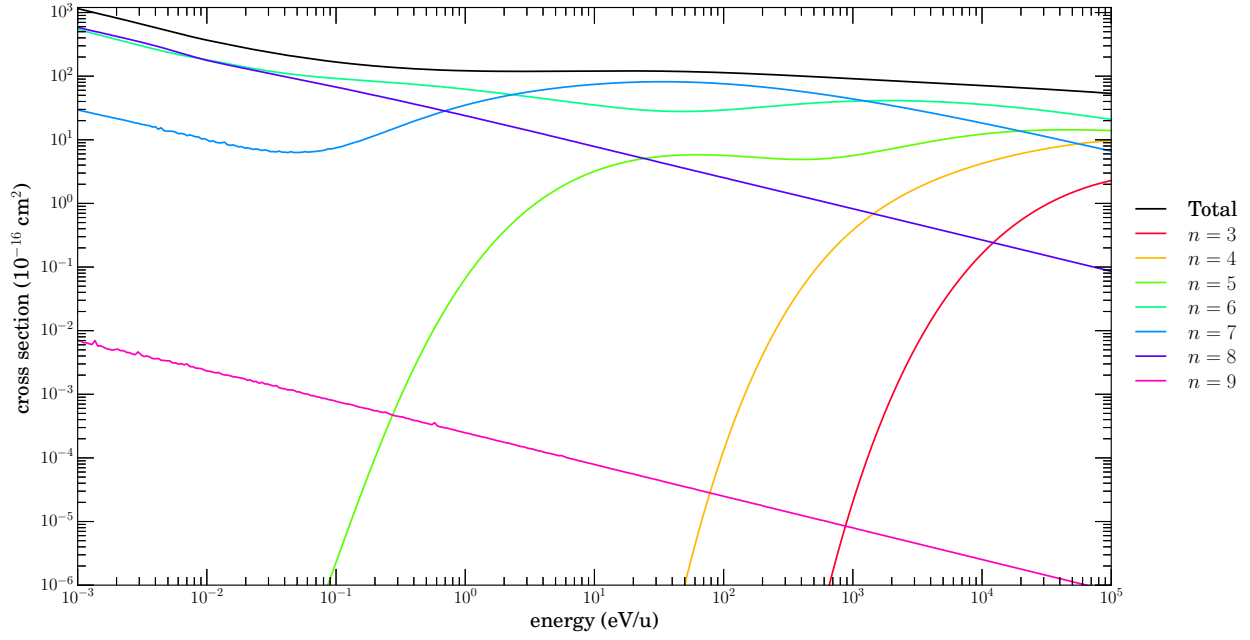
Figure 4.9 $Fe^{9+}+CO_2 \rightarrow Fe^{9+}+CO_2^+$ MCLZ n-resolved cross sections.
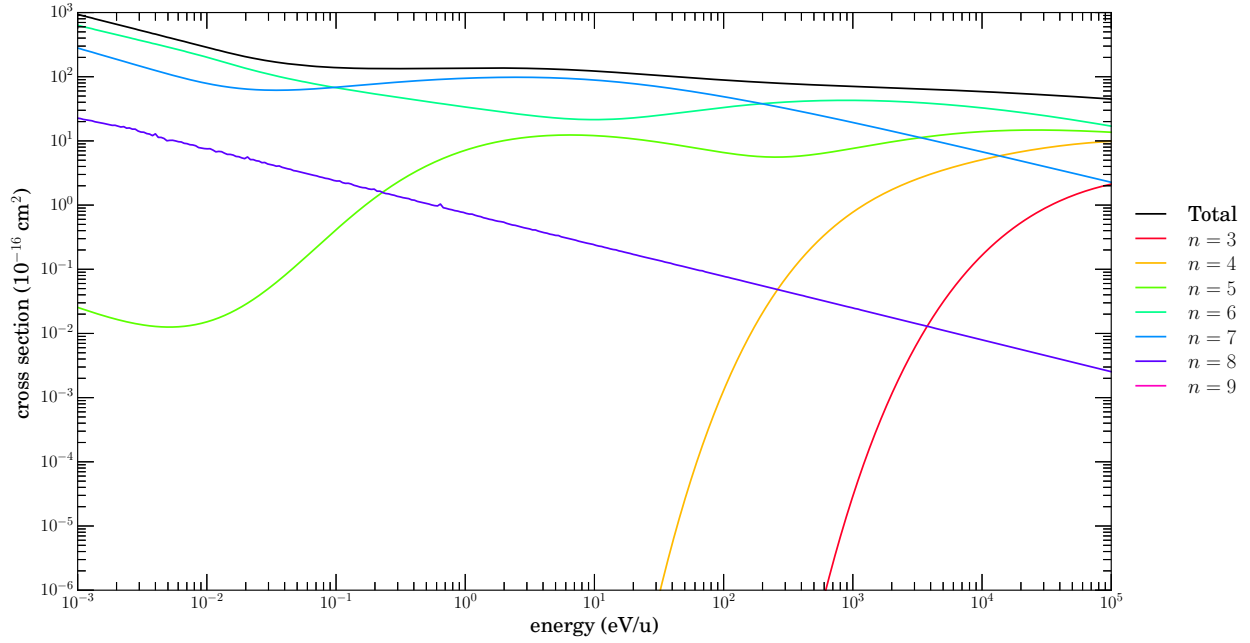
Figure 4.10 $Fe^{9+}+N_2 \rightarrow Fe^{8+}+N_2^+$ MCLZ n-resolved cross sections.

4.3 Fe^{8+}
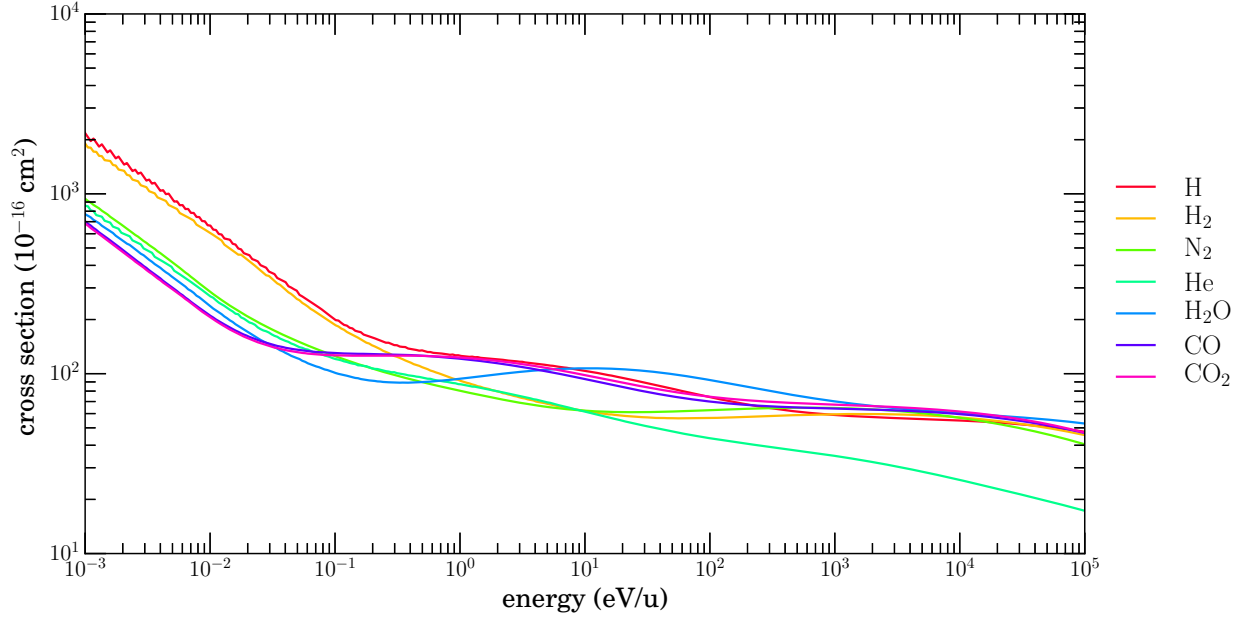
Figure 4.11 $\text{Fe}^{8+}+X{\rightarrow}\text{Fe}^{7+}+X^+$ MCLZ total cross sections.

The energies are calculated from the estimated values of μ, and cross sections are obtained from these energies using the MCLZ method. Plots of these cross sections are shown in Figures 4.11–4.18. Comparisons are made with data available from Simcic et al. (2010a,b), and the results are in agreement. For those systems where no cross sectional data are available, the method used is shown to be sufficiently accurate for Ne and Mg ionic systems (Lyons et al. 2017) in the energy ranges which are presented here.
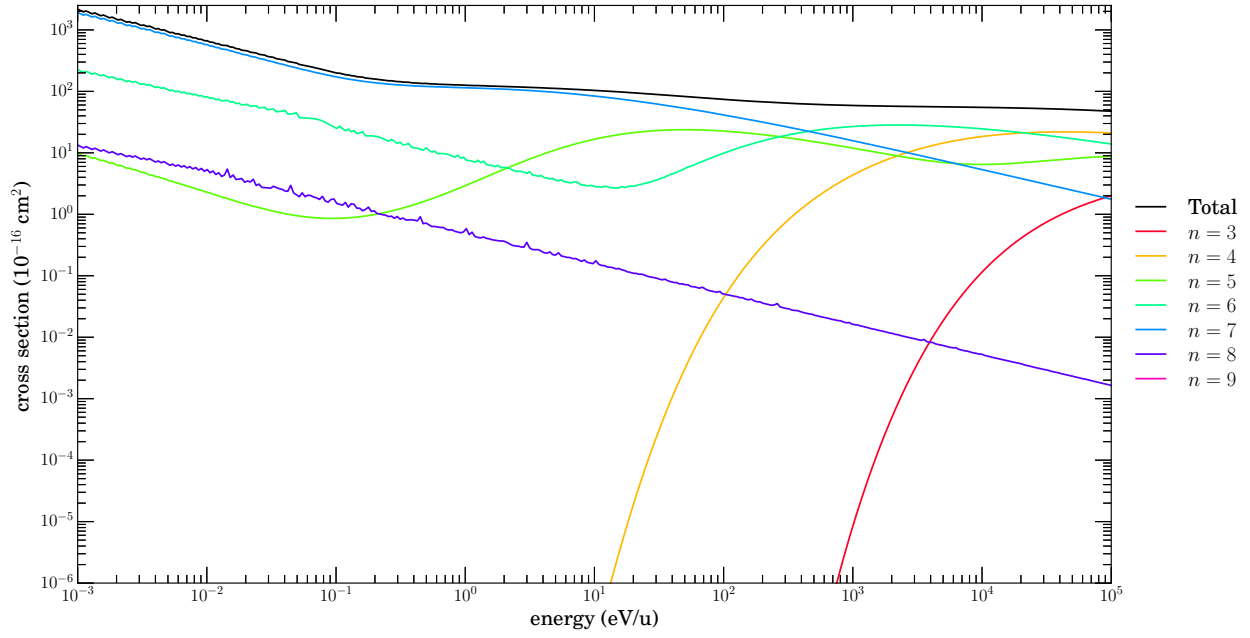
Figure 4.12 $Fe^{8+}+H\rightarrow Fe^{7+}+H^+$ MCLZ n-resolved cross sections; the dominamt channel is n=7 up to
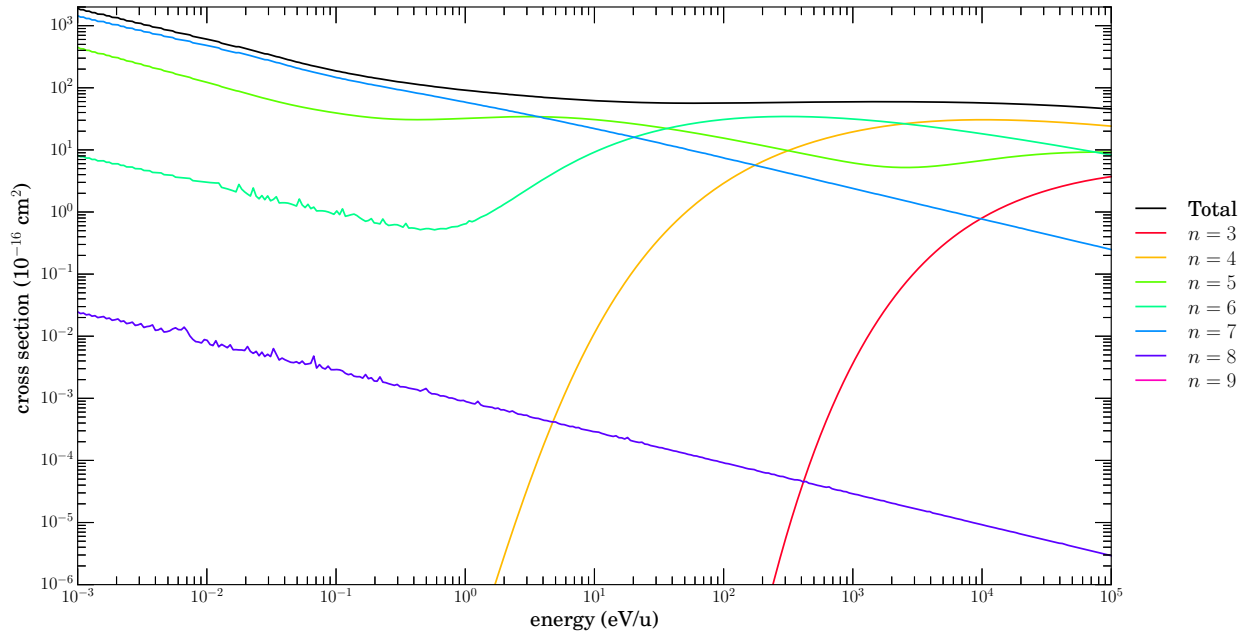
Figure 4.13 $Fe^{8+}+H_2\rightarrow Fe^{7+}+H_2^+$ MCLZ n-resolved cross sections..
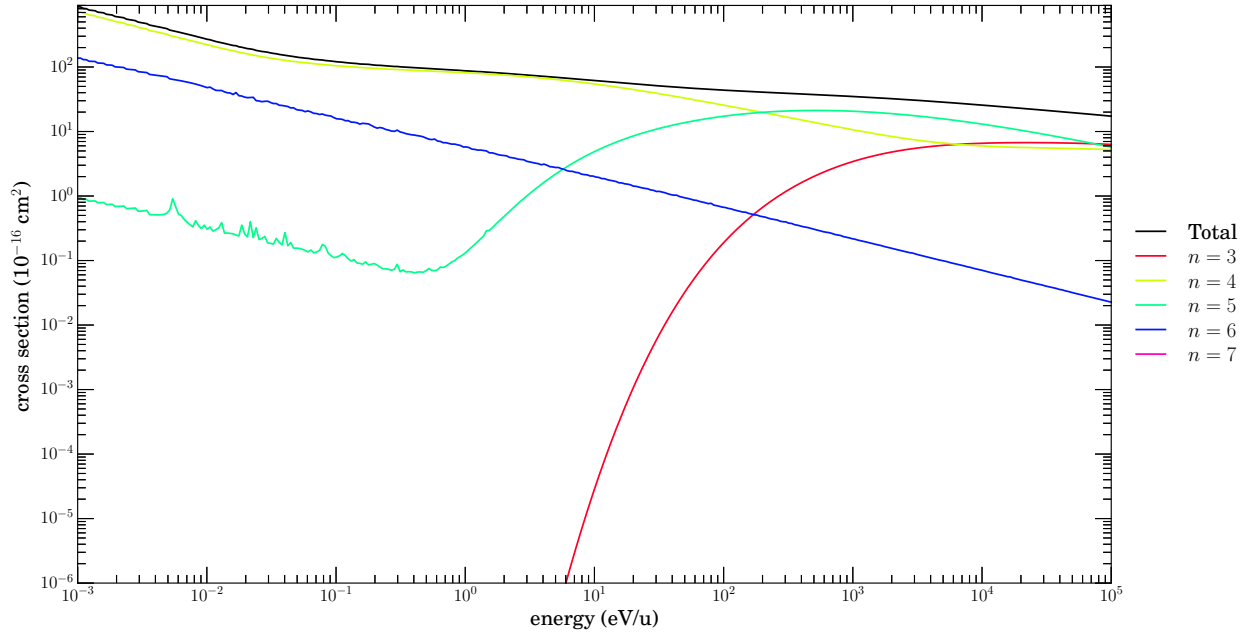
Figure 4.14 $Fe^{8+}+He \rightarrow Fe^{7+}+He^+$ MCLZ n-resolved cross sections.
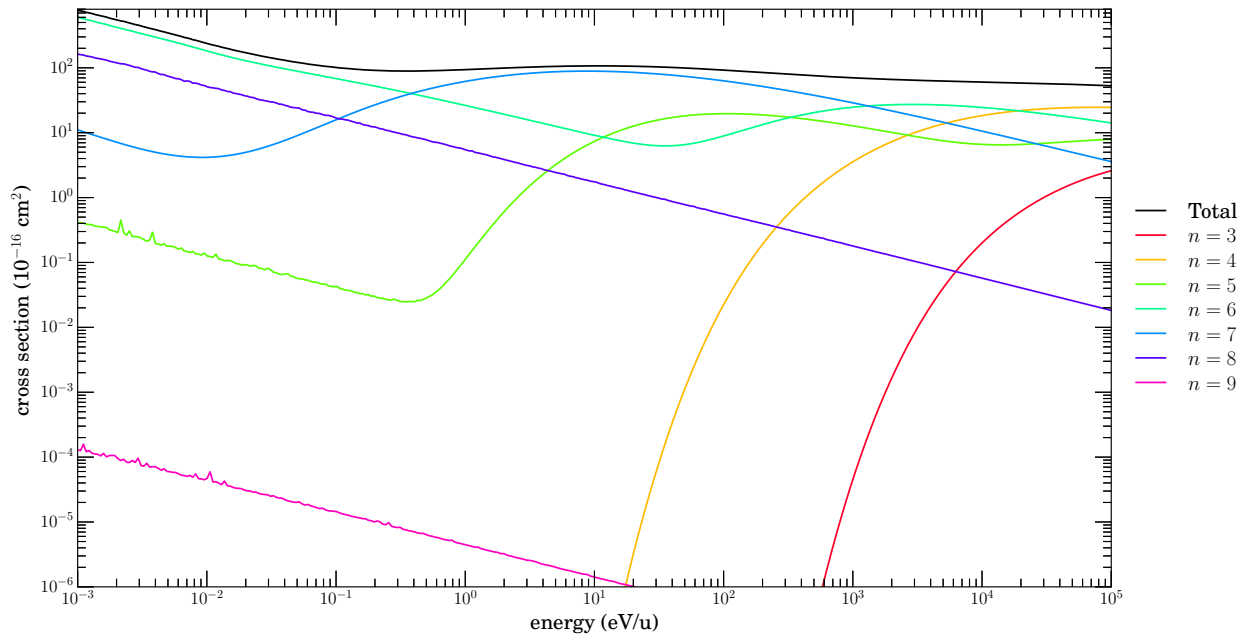
Figure 4.15 $Fe^{8+}+H_2O \rightarrow Fe^{7+}+H_2O^+$ MCLZ n-resolved cross sections.
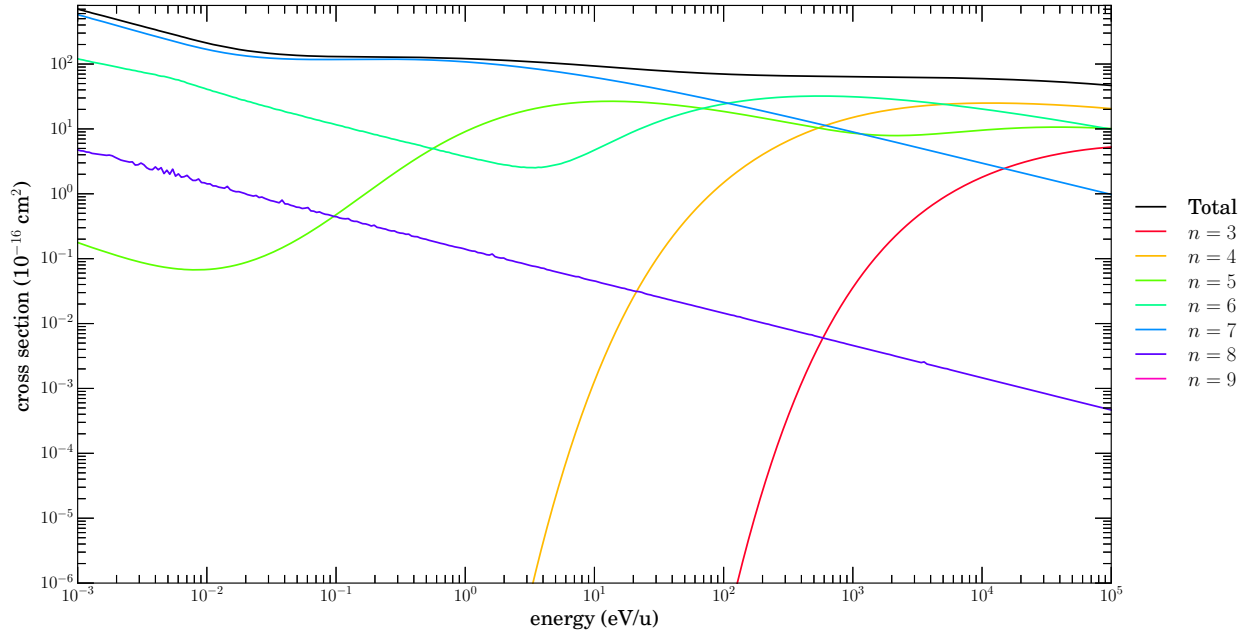
Figure 4.16 $Fe^{8+}+CO \rightarrow Fe^{7+}+CO^+$ MCLZ n-resolved cross sections.
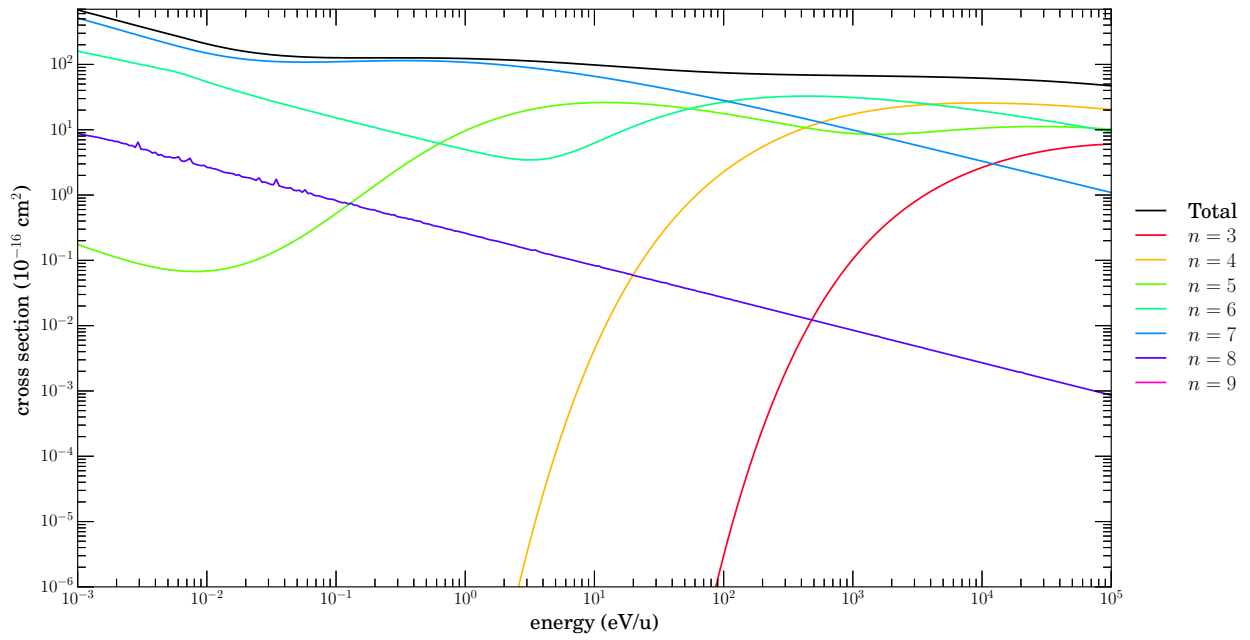
Figure 4.17 $Fe^{8+}+CO_2 \rightarrow Fe^{7+}+CO_2^+$ MCLZ n-resolved cross sections.
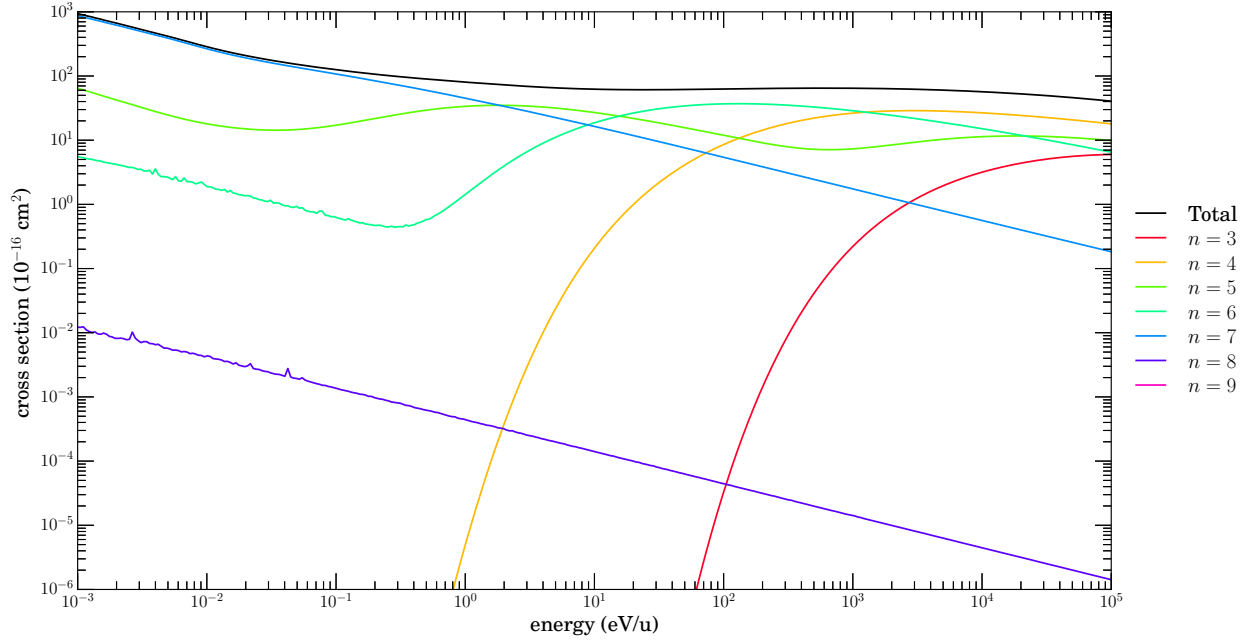
Figure 4.18 $Fe^{8+}+N_2 \rightarrow Fe^{7+}+N_2^+$ MCLZ n-resolved cross sections.

4.4 Tables

Table 4.1.   Fe VIII (Fe^{7+}) NIST Atomic Energies

Configuration	Term	J	Level (cm^{-1})	Term Energy
$3p^63d$	^{2}D	$^3/_2$	0	0
		$^5/_2$	1836	
$3p^5(^2$P$^\circ)3d^2(^1$G$)$	^{2}F$^\circ$	$^5/_2$	431250	432037
		$^7/_2$	434555	
$3p^5(^2$P$^\circ)3d^2(^1$D$)$	^{2}F$^\circ$	$^7/_2$	447658	451575
		$^5/_2$	459367	
$3p^5(^2$P$^\circ)3d^2(^1$S$)$	^{2}P$^\circ$	$^3/_2$	508518	511518
		$^1/_2$	520822	
$3p^64p$	^{2}P$^\circ$	$^1/_2$	510277	512691
		$^3/_2$	515550	
$3p^5(^2$P$^\circ)3d^2(^3$F$)$	^{2}F$^\circ$	$^5/_2$	535909	538988
		$^7/_2$	541755	
$3p^5(^2$P$^\circ)3d^2(^3$P$)$	^{2}P$^\circ$	$^1/_2$	591964	592988
		$^3/_2$	595152	
$3p^5(^2$P$^\circ)3d^2(^3$F$)$	^{2}D$^\circ$	$^5/_2$	596463	595656
		$^3/_2$	597065	
$3p^64f$	2F$^\circ$	$^5/_2$	763703	762656
		$^7/_2$	763799	
$3p^53d(^3$P$^\circ)4s$	^{2}P$^\circ$	$^1/_2$	837661	840005
		$^3/_2$	842829	
$3p^53d(^3$P$^\circ)4s$	^{4}F$^\circ$	$^7/_2$	847145	848229
		$^5/_2$	849899	
		$^3/_2$	852849	
$3p^53d(^3$F$^\circ)4s$	^{2}F$^\circ$	$^7/_2$	855100	856362
		$^5/_2$	860615	
$3p^53d(^3$D$^\circ)4s$	^{4}D$^\circ$	$^7/_2$	874711	875134

Table 4.1 (cont'd)

Configuration	Term	J	Level (cm^{-1})	Term Energy
		$5/2$	876765	
		$3/2$	877476	
		$1/2$	878264	
$3p^53d(^1\text{D}^\circ)4s$	$^2\text{D}^\circ$	$5/2$	879021	878849
		$3/2$	881345	
$3p^53d(^1\text{F}^\circ)4s$	$^2\text{F}^\circ$	$5/2$	884331	884940
		$7/2$	887325	
$3p^53d(^3\text{D}^\circ)4s$	$^2\text{D}^\circ$	$3/25$	889113	889051
		$5/2$	890845	
$3p^65f$	$^2\text{F}^\circ$	$5/2$	927059	925982
		$7/2$	927102	
$3p^66f$	$^2\text{F}^\circ$	$5/2$	1016560	1015464
		$7/2$	1016570	
$3p^67f$	$^2\text{F}^\circ$	$5/2$	1069873	1068861
		$7/2$	1070029	
Fe IX ($3p^{61}\text{S}_0$)	Limit	—	1218380.1	

Table 4.2.   Fe VIII (Fe^{7+}) NIST Singly-Excited State Term Energies

Configuration	Term	Term Energy
$3p^63d$	^2D	0
$3p^64p$	$^2\text{P}^\circ$	512691
$3p^64f$	$^2\text{F}^\circ$	762656
$3p^65f$	$^2\text{F}^\circ$	925982
$3p^66f$	$^2\text{F}^\circ$	1015464
$3p^67f$	$^2\text{F}^\circ$	1068861

Table 4.3. Fe VIII (Fe^{7+}) Term Energies: Estimated and NIST

Valence Electron	Term	Term Energy
$3d$	^{2}D	0
$3d$	^{2}F$^\circ$	432037
$3d$	^{2}F$^\circ$	451575
$4s$	^{2}S	497445
$3d$	^{2}P$^\circ$	511518
$4p$	^{2}P$^\circ$	512691
$4d$	^{2}D	530760
$3d$	^{2}F$^\circ$	538988
$3d$	^{2}P$^\circ$	592988
$3d$	^{2}D$^\circ$	595656
$5s$	^{2}S	756060
$4f$	^{2}F$^\circ$	762656
$5p$	^{2}P	765836
$5d$	^{2}D	777424
$4s$	^{2}P$^\circ$	840005
$4s$	^{2}F$^\circ$	856362
$4s$	^{2}D$^\circ$	878849
$4s$	^{2}F$^\circ$	884940
$4s$	^{2}D$^\circ$	889051
$6s$	^{2}S	896896
$6p$	^{2}P	903695
$6d$	^{2}D	911752
$5f$	^{2}F$^\circ$	925982
$7s$	^{2}S	981963
$7p$	^{2}P	986962
$7d$	^{2}D	992888

Table 4.3 (cont'd)

Valence Electron	Term	Term Energy
$6f$	$^2F^\circ$	1015464
$8s$	^2S	1037244
$8p$	^2P	1041074
$8d$	^2D	1045614
$5g$	^2G	1051250
$7f$	$^2F^\circ$	1068861
$9s$	^2S	1075180
$9p$	^2P	1078209
$9d$	^2D	1081798
$6g$	^2G	1102163
$8f$	$^2F^\circ$	1103894
$9f$	$^2F^\circ$	1127872
$7g$	^2G	1132915
$8g$	^2G	1152899
$6h$	^2H	1155447
$9g$	^2G	1166613
$7h$	^2H	1172100
$8h$	^2H	1182921
$9h$	^2H	1190348
$7i$	^2I	1192789
$8i$	^2I	1198773
$9i$	^2I	1202880
$8k$	^2K	1206196
$9k$	^2K	1208748
$9l$	^2L	1213309

54

Table 4.4.   Fe IX (Fe^{8+}) NIST Atomic Energies

Configuration	Term	J	Level	Term Energy
$3s^23p^6$	^{1}S	0	0	0
$3s^23p^53d$	^{3}P$^\circ$	0	405772	411007
		1	408315.1	
		2	413669.2	
$3s^23p^53d$	^{3}F$^\circ$	4	425809.8	428883.7
		3	429310.9	
		2	433818.8	
$3s^23p^53d$	^{3}D$^\circ$	3	455612.2	458948
		1	460616	
		2	462616.6	
$3s^23p^53d$	^{1}D$^\circ$	2	456752.7	456752.7
$3s^23p^53d$	^{1}F$^\circ$	3	465828.4	465828.4
$3s^23p^53d$	^{1}P$^\circ$	1	584546	584546
$3s3p^63d$	^{3}D	1	726734	728036
		2	727560	
		3	728935	
$3s3p^63d$	^{1}D	2	749871	749871
$3s^23p^5(^2$P$^\circ_{3/2})4s$	$(^3/_2, ^1/_2)^\circ$	1	950500	950500
$3s^23p^5(^2$P$^\circ_{1/2})4s$	$(^1/_2, ^1/_2)^\circ$	1	965570	965570
$3s^23p^54d$	^{3}P$^\circ$	1	1198220	1198220
$3s^23p^54d$	^{1}P$^\circ$	1	1213150	1213150
$3s^23p^5(^2$P$^\circ_{3/2})4f$	$^2[^3/_2]$	1	1300920	1302120
		2	1302840	
$3s^23p^5(^2$P$^\circ_{3/2})4f$	$^2[^9/_2]$	5	1304600	1305374

Table 4.4 (cont'd)

Configuration	Term	J	Level	Term Energy
		4	1306320	
$3s^2 3p^5(^2P^\circ_{3/2})4f$	$^2[5/2]$	3	1305760	1305760
$3s^2 3p^5(^2P^\circ_{3/2})4f$	$^2[7/2]$	3	1310160	1311054
		4	1311750	
$3s^2 3p^5(^2P^\circ_{1/2})4f$	$^2[5/2]$	3	1323660	1323660
$3s^2 3p^5(^2P^\circ_{1/2})4f$	$^2[7/2]$	3	1324720	1324765
		4	1324800	
$3s^2 3p^5(^2P^\circ_{3/2})5s$	$(^3/_2, ^1/_2)^\circ$	1	1358140	1358140
$3s3p^6 4p$	$^1P^\circ$	1	1371910	1371910
$3s^2 3p^5(^2P^\circ_{1/2})5s$	$(^1/_2, ^1/_2)^\circ$	1	1372670	1372670
Fe X $(3p^5\,^2P^\circ_{3/2})$	Limit	—	1884000.3	

Table 4.5.   Fe IX (Fe^{8+}) Singlet Term Energies: Estimated and NIST

Valence Electron	Term	Term Energy
$3p$	^1S	0.00000000E+00
$3d$	$^1D^\circ$	4.56752700E+05
$3d$	$^1F^\circ$	4.65828400E+05
$3d$	$^1P^\circ$	5.84546000E+05
$3d$	^1D	7.49871000E+05
$4s$	$(^1/_2, ^1/_2)^\circ$	9.65570000e+05
$4d$	$^1P^\circ$	1.21315000E+06
$4f$	$^2[5/2]$	1.32366000E+06
$4f$	$^2[7/2]$	1.32476500E+06
$5p$	^1P	1.36958893E+06
$5d$	^1D	1.37019116E+06
$4p$	$^1P^\circ$	1.37191000E+06
$5s$	$(^1/_2, ^1/_2)^\circ$	1.37267000E+06
$5f$	^1F	1.51143825E+06
$6s$	^1S	1.52630306E+06
$6p$	^1P	1.52677018E+06
$6d$	^1D	1.52718840E+06
$5g$	^1G	1.55691692E+06
$7s$	^1S	1.62120233E+06
$7p$	^1P	1.62154552E+06
$7d$	^1D	1.62185278E+06
$6f$	^1F	1.62527665E+06
$6g$	^1G	1.65685906E+06
$8s$	^1S	1.68279560E+06
$8p$	^1P	1.68305836E+06
$8d$	^1D	1.68329361E+06

Table 4.5 (cont'd)

Valence Electron	Term	Term Energy
6h	^{1}H	1.68795448E+06
7f	^{1}F	1.69391762E+06
7g	^{1}G	1.71712102E+06
9s	^{1}S	1.725023749e+06
9p	^{1}P	1.72523136E+06
9d	^{1}D	1.72541723E+06
8f	^{1}F	1.73846825E+06
7h	^{1}H	1.73996664E+06
7i	^{1}I	1.74638158E+06
8g	^{1}G	1.75623335E+06
9f	^{1}F	1.76901201E+06
8h	^{1}H	1.77372453E+06
8i	^{1}I	1.77863597E+06
9g	^{1}G	1.78304864E+06
8k	^{1}K	1.79096325E+06
9h	^{1}H	1.79686883E+06
9i	^{1}I	1.80074947E+06
9k	^{1}K	1.81048954E+06
9l	^{1}L	1.82171930E+06

Table 4.6. Fe IX (Fe^{8+}) Triplet Term Energies: Estimated and NIST

Valence Electron	Term	Term Energy
$3d$	^{3}P$^\circ$	4.11007000E+05
$3d$	^{3}F$^\circ$	4.28883700E+05
$3d$	^{3}D$^\circ$	4.58948000E+05
$3d$	^{3}D	7.28036000E+05
$4s$	$(^3/_2, ^1/_2)^\circ$	9.50500000E+05
$4d$	^{3}P$^\circ$	1.19822000E+06
$4p$	^{3}P	1.29046568E+06
$4f$	$^2[^3/_2]$	1.30212000E+06
$4f$	$^2[^9/_2]$	1.30537400E+06
$4f$	$^2[^5/_2]$	1.30576000E+06
$4f$	$^2[^7/_2]$	1.31105400E+06
$5p$	^{3}P	1.35624063E+06
$5s$	$(^3/_2, ^1/_2)^\circ$	1.35814000E+06
$5d$	^{3}D	1.35814943E+06
$5f$	^{3}F	1.50413814E+06
$6s$	^{3}S	1.51701127E+06
$6p$	^{3}P	1.51750053E+06
$6d$	^{3}D	1.51882609E+06
$5g$	^{3}G	1.55070963E+06
$7s$	^{3}S	1.61437571E+06
$7p$	^{3}P	1.61473516E+06
$7d$	^{3}D	1.61570904E+06
$6f$	^{3}F	1.62020713E+06
$6g$	^{3}G	1.65254845E+06
$8s$	^{3}S	1.67756897E+06
$8p$	^{3}P	1.67784418E+06

Table 4.6 (cont'd)

Valence Electron	Term	Term Energy
$8d$	^{3}D	1.67858980E+06
$6h$	^{3}H	1.68446797E+06
$7f$	^{3}F	1.69019308E+06
$7g$	^{3}G	1.71395404E+06
$9s$	^{3}S	1.72089407E+06
$9p$	^{3}P	1.72111151E+06
$9d$	^{3}D	1.72170065E+06
$8f$	^{3}F	1.73561664E+06
$7h$	^{3}H	1.73740512E+06
$7i$	^{3}I	1.74386209E+06
$8g$	^{3}G	1.75380863E+06
$9f$	^{3}F	1.76675889E+06
$8h$	^{3}H	1.77176336E+06
$8i$	^{3}I	1.77670698E+06
$9g$	^{3}G	1.78113281E+06
$8k$	^{3}K	1.78937009E+06
$9h$	^{3}H	1.79531926E+06
$9i$	^{3}I	1.79922533E+06
$9k$	^{3}K	1.80923075E+06
$9l$	^{3}L	1.82078846E+06

Table 4.7.   Degeneracy Factors

State	Factor
$^1\Sigma$	0.08333
$^1\Pi$	0.1667
$^3\Sigma$	0.2500
$^3\Pi$	0.5000

CHAPTER 5

NE^{9+}+H USING MOCC

[1]

5.1   METHOD

5.2   RESULTS

---

[1]Lyons, David A., and Stancil, Phillip C., 2019. To be submitted to *The Astrophysical Journal*.

Conclusions

6.1 MCLZ: $Ne^{(8-10)+}$ AND $Mg^{(8-12)+}$

Using the multichannel Landau–Zener method, state-resolved CX cross sections were computed for highly charged Ne and Mg ions colliding with H and He. It was found that the MCLZ method can provide reasonable SEC cross sections for energies below 10 keV/u for the dominant capture channels. Comparison to previous work was primarily limited to Ne^{10+}+H and a handful of results for Ne^{9+} and Ne^{8+}. Some of the other less dominant channels do not agree as closely with other theoretical and experimental data as do the dominant channels, while prior results for the Mg ions considered here are completely lacking.

6.2 MCLZ: $Fe^{(8-9)+}$

Cross sections were calculated for ionic systems Fe^{8+} and Fe^{9+} colliding with neutral atoms and molecules H, H_2, He, H_2O, CO, CO_2, and N_2, for single election capture. Excitation energies were estimated where data were not provided by NIST or other sources. These estimations were based on a version of the Quantum Defect method and graphical methods. The estimations of excitation energies should be accurate to two significant digits.

The MCLZ method was shown to be reasonably accurate for energy ranges below 10 KeV/u for dominant capture channels with Ne and Mg ions (Lyons et al. 2017) and 3. It is therefore assumed that the accuracy of the method for $Fe^{(8-9)+}$ is consistent with that study.

6.3 MOCC: Ne^{9+}+H

Stüeckelberg

The cross sections computed here were generated with the MCLZ package *Stüeckelberg* written by the author using the C language and designed to be highly automated, efficient, and modular. The user is required to only provide asymptotic atomic ion energies to *Stüeckelberg*, but a careful application of Wigner-Witmer rules to select final states consistent with allowed transitions is the user's responsibility. The code can be downloaded from https://www.physast.uga.edu/ambds/ along with documentation and a start-up guide.

Within the CXDatabase directory one will find the input files for *Stüeckelberg* and various output files including lists of avoided-crossings as well as n-, $n\ell$-, and $n\ell S$-resolved cross sections. For bare ions, $n\ell$ cross sections are given using the low-energy and statistical distribution functions, but other ℓ-distribution functions can be applied by the user to the n-resolved cross section files. Cross sections for additional collision pairs and/or obtained by other theoretical methods are expected to be routinely added. The cross sections will also be available on the UGA Charge Transfer Database (https://www.physast.uga.edu/ugacxdb/).

Bibliography

Abramov, V. A., Baryshnikov, F. F., and Lisitsa, V. S. (1978). *Charge transfer between hydrogen atoms and the nuclei of multicharged ions with allowance for the degeneracy of the final states. Sov. Phys. JETP*, 47:469–477.

Ali, R., Neill, P. A., Beiersdorfer, P., Harris, C. L., Schultz, D. R., and Stancil, P. C. (2010). *Critical test of simulations of charge-exchange-induced x-ray emission in the solar system. ApJ*, 716:L95–L98.

Bendahman, M., Bliman, S., Dousson, S., Hitz, D., Gayet, R., Hanssen, J., Harel, C., and Salin, A. (1985). *Electron capture from atomic hydrogen by multiply charged ions in low energy collisions. J. De Physique*, 46:561–572.

Butler, S. E. and Dalgarno, A. (1980). *Charge transfer of multiply charged ions with hydrogen and helium: Landau-Zener calculations. ApJ*, 241:838–843.

Connerade, J. P. (1998). *Highly Excited Ions.* Cambridge University Press.

Cox, D. P. (1998). *Modeling the Local Bubble.* In Breitschwerdt, D., Freyberg, M. J., and Trümper, J., editors, *The Local Bubble and Beyond: Lyman-Spitzer-Colloquium (Lecture Notes in Physics)*, pages 121–131. Berlin:Springer, 1998 edition.

Cravens, T. E. (2000). *Heliospheric x-ray emission associated with charge transfer of the solar wind with interstellar neutrals. ApJ*, 532(2):L153–L156.

Cravens, T. E., Howell, E., Waite, Jr., J. H., and Gladstone, G. R. (1995). *Auroral oxygen precipitation at Jupiter. Journal of Geophysical Research*, 100:17153–17162.

Cumbee, R. S., Henley, D. B., Stancil, P. C., Shelton, R. L., Nolte, J. L., Wu, Y., and Schultz, D. R. (2014). *Can charge exchange explain anomalous soft x-ray emission in the Cygnus Loop? ApJ*, 787(2):L31.

Cumbee, R. S., Liu, L., Lyons, D., Schultz, D. R., Stancil, P. C., Wang, J. G., and Ali, R. (2016). *Ne X X-ray Emission due to Charge Exchange in M82. Monthly Notices of the Royal Astronomical Society*, 458(4):3554–3560.

Errea, L. F., Illescas, C., Méndez, L., Pons, B., Riera, A., and Suárez, J. (2004). *Accuracy of the classical trajectory Monte Carlo method for electron capture in Li^{3+} and $Ne^{10+}+H(1s)$ collisions. Phys. Rev. A*, 70:052713.

Fabian, A. C., Sanders, J. S., Williams, R. J. R., Lazarian, A., Ferland, G. J., and Johnstone, R. M. (2011). *The energy source of the filaments around the giant galaxy NGC 1275. Monthly Notices of the Royal Astronomical Society*, 417:172–177.

Greenwood, J. B., Williams, I. D., Smith, S. J., and Chutjian, A. (2001). *Experimental investigation of the processes determining x-ray emission intensities from charge-exchange collisions. Phys. Rev. A*, 63:062707.

Grozdanov, T. P. (1980). *Classical model for electron capture in collisions of highly charged, fully stripped ions with hydrogen atoms. Journal of Physics B: Atomic Molecular Physics*, 13:3835–3847.

Janev, R. K., Belić, D. S., and Bransden, B. H. (1983). *Total and partial cross sections for electron capture in collisions of hydrogen atoms with fully stripped ions. Phys. Rev. A*, 28:3:1293–1302.

Katsuda, S., Tsunemi, H., Mori, K., Uchida, H., Kosugi, H., Kimura, M., Nakajima, H., Takakura, S., Petre, R., Hewitt, J. W., and Yamaguchi, H. (2011). *Possible charge-exchange x-ray emission in the Cygnus Loop detected with Suzaku. The Astrophysical Journal*, 730(1):24.

Kramida, A., Ralchenko, Y., Reader, J., and NIST ASD Team (2018). NIST Atomic Spectra Database (ver. 5.6.1), [Online]. Available: `https://physics.nist.gov/asd` [2015, April 16]. National Institute of Standards and Technology, Gaithersburg, MD.

Krasnopolsky, V. A., Greenwood, J. B., and Stancil, P. C. (2004). *X-Ray and extreme ultraviolet emissions from comets. Space Sci. Rev.*, 113:271–374.

Landau, L. D. (1932). *A theory of energy transfer II. Phys. Zts. Sowjetunion*, 2:46.

Lisse, C. M., Dennerl, K., Englhauser, J., Harden, M., Marshall, F. E., Mumma, M. J., Petre, R., Pye, J. P., Ricketts, M. J., Schmitt, J., Trümper, J., and West, R. G. (1996). *Discovery of x-ray and extreme ultraviolet emission from comet C/Hyakutake 1996 B2. Science*, 274(5285):205–209.

Lyons, D., Cumbee, R. S., and Stancil, P. C. (2017). *Charge Exchange between Ne and Mg Ions and H and He. ApJS*, 232(2):27–43.

Maynard, G., Janev, R. K., and Katsonis, K. (1992). *Electron capture and ionization in collisions of multicharged neon ions with atomic hydrogen. Journal of Physics B: Atomic, Molecular and Optical Physics*, 25(2):437–444.

Meyer, F. W., Howald, A. M., Havener, C. C., and Phaneuf, R. A. (1985). *Low-energy total-electron-capture cross sections for fully stripped and H-like projectiles incident on H and H_2. Phys. Rev. A*, 32:3310–3318.

Mullen, P. D., Cumbee, R. S., Lyons, D., and Stancil, P. C. (2016). *Charge exchange-induced x-ray emission of Fe xxv and Fe xxvi via a streamlined model. ApJS*, 224(2):31.

Nakamura, H. (2002). *Nonadiabatic Transition.* World Scientific Publishing Co Pte Ltd.

Olson, R. E. and Salop, A. (1977). *Charge-transfer and impact-ionization cross sections for fully and partially stripped positive ions colliding with atomic hydrogen. Phys. Rev. A*, 16:531–541.

Perez, J. A., Olson, R. E., and Beiersdorfer, P. (2001). *Charge transfer and x-ray emission reactions involving highly charged ions and neutral hydrogen. Journal of Physics B: Atomic, Molecular and Optical Physics*, 34(15):3063–3072.

Schultz, D. R. and Kristić, P. S. (1996). *Atomic and Plasma-Material Interaction Data for Fusion. Supplement to the Journal Nuclear Fusion*, 16:173.

Schwerdtfeger, P. and Nagle, J. K. (2018). *2018 Table of static dipole polarizabilities of the neutral elements in the periodic table. Molecular Physics*, 0(0):1–26.

Simcic, J., Schultz, D. R., Mawhorter, R. J., Greenwood, J. B., Winstead, C., McKoy, B. V., and Chutjian, S. J. S. A. (2010a). *Measurement and Calculation of Absolute Single and Multiple Charge Exchange Cross Sections for Fe^{q+} Ions Impacting H_2O. ApJ*, 722:425–439.

Simcic, J., Schultz, D. R., Mawhorter, R. J., Čadež, I., Greenwood, J. B., Chutjian, A., Smith, S. J., and Lisse, C. M. (2010b). *Measurement of absolute single and multiple charge exchange cross sections for Fe^{q+} ions impacting CO and CO_2. Phys. Rev. A*, 81:062715.

Smith, R. K., Foster, A. R., Edgar, R. J., and Brickhouse, N. S. (2014). *Resolving the origin of the diffuse soft x-ray background. ApJ*, 787(1):77.

Stüeckelberg, E. C. G. (1932). *Theory of Inelastic Collisions between Atoms. Helvetica Physica Acta*, 5:369–423.

Taulbjerg, K. (1986). *Reaction windows for electron capture by highly charged ions. Journal of Physics B: Atomic and Molecular Physics*, 19(10):L367–L372.

Wigner, E. and Witmer, E. E. (1928). *Über die Struktur der zweiatomigen Molekelspektren nach der Quantenmechanik. Zeitschrift fur Physik*, 51:859.

Zener, C. (1932). *Non-adiabatic crossing of energy levels. Proceedings of the Royal Society of London. Series A, Containing Papers of a Mathematical and Physical Character*, 137:696–702.